Research Article | Vol. 30, No. 11 / 23 May 2022 / Optics Express 19246

Optics EXPRESS

# Diffraction and thermal effect of a Bessel-Gaussian laser for Ag nanoparticle deposition

TIANYI LI,[1] KRISTOPHER O. DAVIS,[2] RANGANATHAN KUMAR,[1] AND ARAVINDA KAR[3,*]

[1]Department of Mechanical and Aerospace Engineering, University of Central Florida, Orlando, Florida 32816, USA
[2]Department of Materials Science and Engineering, University of Central Florida, Orlando, Florida 32816, USA
[3]The College of Optics and Photonics, University of Central Florida, Orlando, Florida 32816, USA
[*]akar@creol.ucf.edu

**Abstract:** Nanoparticles are known to sinter at much lower temperatures than the corresponding bulk or micro size particles. A laser-assisted sintering process is considered in this study to sinter Ag nanoparticles by dispensing Ag paste onto an indium tin oxide-coated Si substrate. The Gaussian beam of a $CO_2$ laser source is propagated through axicon and biconvex lenses, and the resulting hollow beam is focused on the Ag paste with a hollow parabolic mirror. A Bessel-Gaussian irradiance distribution is obtained at the focal plane of the parabolic mirror due to the interference of the hollow laser cone. The Fresnel diffraction approximation is considered to determine the phasor of the laser and an analytical approach is implemented to calculate the irradiance distribution of the Bessel-Gaussian beam. This irradiance distribution is utilized as a heat source in a heat conduction model and the temperature distribution is analyzed for thin Ag films formed during the laser sintering of Ag nanoparticles. An analytical expression is obtained for the temperature distribution by solving the heat conduction equation using Fourier transform for finite media. The widths of the deposited Ag lines are predicted from the temperature profiles and the model predictions compare well with the experimental results. The isotherms are found to be geometrically noncongruent with convex and concave tips depending on the locally maximum and minimum irradiances of the Bessel-Gaussian beam, respectively. The convex and concave tips, however, appear in the same isotherm for sufficiently high substrate speed relative to the laser beam.



## 1. Introduction

The Gaussian beams are widely used for laser-assisted manufacturing and materials processing [1]. This type of beams exhibits diffractive spreading, resulting in rapid decrease of the peak irradiance as a function of the longitudinal, that is the beam propagation, distance [2]. Also, the irradiance decreases monotonically in the transverse, that is the radial, direction and, therefore, heats the substrates with monotonically decreasing temperature distribution. Special beam shaping optics are needed to modify the Gaussian beam profile for creating localized peak temperatures. The Bessel beams, on the other hand, provide a natural means of heating the substrates with undulating temperature distribution. The zeroth order Bessel function of the first kind, $J_0$, represents the electric field amplitude of a nondiffracting zeroth order Bessel beam. Since the irradiance is proportional to the square of the electric field amplitude and the *Jo* function is not square integrable, an integration of the irradiance over the entire transverse plane would yield infinite laser power in the beam [3,4]. Physically an ideal zeroth order Bessel beam consists of an infinite number of circular rings around a central maximum irradiance and

#455313 https://doi.org/10.1364/OE.455313
Journal © 2022 Received 7 Feb 2022; revised 8 Apr 2022; accepted 22 Apr 2022; published 18 May 2022

Optics EXPRESS

the energy in each ring is approximately equal to the energy contained in the central ring. The energy of such a beam would be infinite which is unrealistic and this ideal beam is, therefore, difficult to achieve in practice. Indebetouw [5] showed that approximately nondiffracting beam can be synthesized using an axicon lens. The irradiance of such approximate Bessel beams varies along the propagation direction [6] and the Rayleigh range is longer than that of a Gaussian beam [7]. Typical laser sources generally produce Gaussian beams which can be passed through axicon and biconvex lenses to form a hollow beam with half-Gaussian irradiance profile. When the hollow beam is focused with a lens, a new pattern is obtained at the focal place for the electric field amplitude which is square integrable and the corresponding beam is known as the Bessel-Gaussian (BG) beam. The formation of BG beams with different irradiance profiles and their heating effects on solid materials have been studied by Zeng et al. [8,9], showing an efficient utilization of laser heating with BG beams of certain irradiance profiles. Recently Castillo-Orozco et al. [10,11] used BG beams to evaporate microdroplets of nanoparticle suspensions and sinter the nanoparticles for depositing thin films on both rigid and flexible substrates.

Lasers offer precise control for spatial and temporal heating of materials with little damage to the substrates. In addition, nanoparticles have better mechanical, electrical, and optical properties as well as lower sintering temperature than to the corresponding bulk materials [12]. Depositing nanomaterials to produce thin lines or films is of interest for fabricating optoelectronic, energy and electronic components [13] such as light-emitting diodes [14], ultra-flexible electrodes [15] and solar cells [16]. Fabrication of nanostructures on flexible and stretchable substrates is also of interest in the development of wearable electronic and photonic devices [17]. Numerous deposition techniques have been studied by others without using lasers. An et al. [18] used layer-by-layer deposition to produce nanosheets of two-dimensional metal carbides in between polymer sheets. Thomas et al. [19] fabricated densely packed micro and nanoscale polymer features using a melt processing approach. Chemically synthesized semiconductor nanowires of ZnO or carbon nanotubes on flexible conductive substrates have been investigated for electronic and photonic device applications [20,21]. Conventional inkjet printing method has been employed to pattern microelectrodes of semiconductor materials on flexible substrates [22]. Shin et al. [23] developed an electrostatic force-assisted Ag paste dispensing technique to print Ag fingers on solar cells. An oven was used in their process to cure the paste and, consequently, the fabrication time was relatively long. Castillo-Orozco [10] employed a Nd:YAG laser BG beam and deposited thin films of metal (Ag) and semiconductor (Si) nanoparticles on flexible substrates. Metallization of the precursor Ag paste to form continuous Ag lines is a crucial step for fabricating efficient Si solar cells [24]. Good electrical contact between Si and Ag lines with low line resistance and high aspect ratio enhances the efficiency of solar cells by reducing resistive and optical losses [25]. The pastes of Ag nanoparticles are used for manufacturing the contact lines for its low sintering temperature compared to the bulk Ag material [26,27].

In the current study, an experimental setup is presented to show certain optical elements that produce a BG beam on the substrate surface. This setup was utilized to deposit Ag lines on indium tin oxide (ITO)-coated silicon substrates using an Ag nanoparticle paste as a precursor. The primary focus of this paper is to study the thermal effect of the BG beam on the temperature distribution in the substrate. For this purpose, an expression is obtained for the irradiance of the BG beam by applying the Fresnel diffraction model, and this irradiance is used as a heat source in a heat conduction model to analytically solve for the temperature distribution. Since the nanoparticles sinter above a certain temperature, this constraint is applied to the temperature distribution to predict the width of the deposited Ag line as an illustration for the practical application of the thermal model. Most of the results have previously been published in a dissertation [28]. Those results are presented in this paper more succinctly by highlighting the similarity between the beam pattern and temperature profiles, and the evolution of different heating regimes under various processing conditions.

Optics EXPRESS

## 2. Experimental setup for BG beam formation and Ag line deposition

Figure 1 illustrates an experimental setup, showing a continuous wave $CO_2$ laser of wavelength $\lambda = 10.6\mu m$ and Gaussian irradiance distribution. This beam is passed through an axicon lens and a biconvex lens to form a hollow beam with outer-half-Gaussian irradiance distribution [8], and then focused with a hollow parabolic mirror on Ag lines, resulting in an irradiance profile that is referred to as the BG beam in this study. One of the advantages of BG beams is that its maximum intensity is much higher than that of Gaussian beams of the same power. Thus, much higher intensity can be applied to materials using BG beams. In addition, the BG beam is useful for deposition processes since it has longer Rayleigh range within which the irradiance distribution does not vary significantly. A stable thermal process, therefore, can be established even if the focal spot is not exactly on the substrate surface. This fault-tolerant feature is beneficial since the height of the Ag line may vary due to mechanical vibration of the linear stage or fluctuations in the flow rate of nanosuspension. The BG beams provide a large tolerance in the height direction to enable sintering the Ag lines uniformly. The mirror is hollow because it has a vertical hole starting from its top surface to the center of the reflective parabolic surface. This mirror with focusing capability, particularly the hole in the parabolic mirror, provides a convenient space to access the laser-material interaction region for measuring temperature using an infrared camera coaxially with the laser beam. Alternatively, the hollow space can be utilized to coaxially dispense nanosuspensions to the center of the beam. The laser spot diameter on the substrate surface was adjusted to be $300\mu m$, which was the smallest spot size in the experiment setup of this study and this size was measured from the illuminated spot on a sensitive paper. From the BG beam profile, the laser irradiance at the beam radius of $150\mu m$ is determined to be one-fifth of the maximum irradiance. The power, $P$, was varied from 2.3W to 11.8W to deposit Ag lines without causing any thermal damage to the silicon substrates used in this study. An Ag nanoparticle suspension, which was 75wt% LIFT (Laser-Induced Forward Transfer) printable silver ink from Sigma-Aldrich, was delivered to an ITO-coated Si substrate using a needle of inner and outer diameters $51\mu m$ and $159\mu m$, respectively. The ink was delivered behind the BG beam and the substrate was moved at the speed $V$ (Fig. 1). The flow rate of the ink, $Q$, was controlled with a syringe pump in the range of 100-200 nL/min and the substrate speed, $V$, was varied from 0.92 mm/s to 6 mm/s for depositing Ag lines under different conditions.

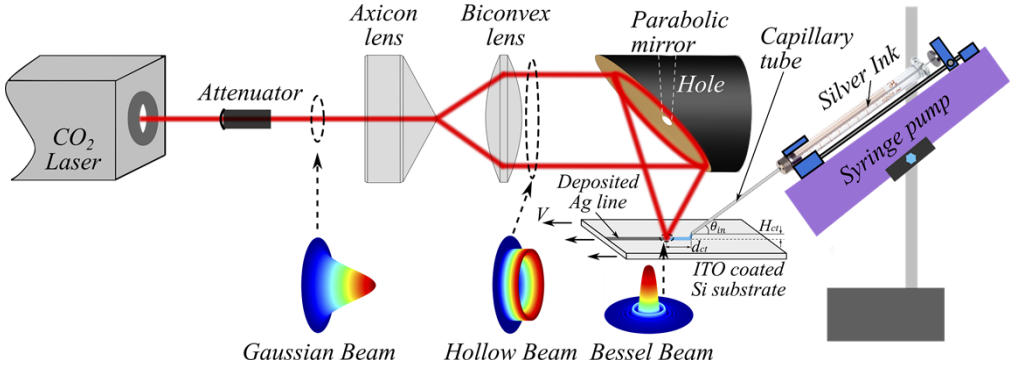


**Fig. 1.** Schematic of optical elements and laser track for Bessel-Gaussian beam formation during silver line deposition on ITO-coated substrates.

The depositions were achieved in two steps, ink drying and nanoparticle sintering. For the case of ink drying, the silver ink was supplied to the substrate with a capillary tube of a syringe pump at the flow rate ($Q$) of 100nL/min while the substrate speed ($V$) was 6mm/s relative to the laser beam. The height ($H_{ct}$) of the tip of the capillary tube and the inclination angle ($\theta_{in}$) of the

Optics EXPRESS

tube were 50μm and 40°, respectively, from the substrate surface. As a liquid ink line is drawn due to the motion of the substrate, the liquid was simultaneously evaporated to dry the line with the laser power ($P_d$) 2.3W. The diameter ($D_L$) of the laser focal spot was 300μm on the substrate surface and the center of the laser beam was ahead of the tip of the capillary tube by a horizontal distance ($d_{ct}$) 1.5mm. After this drying step, the Ag nanoparticles were sintered with the laser power ($P$) 11.8W and $V$ at 1mm/s. The width and height of the sintered Ag lines were measured with an optical microscope at 500 magnification and an optical profilometer respectively.

## 3. Methodology

### 3.1. Diffraction modeling of Bessel- Gaussian irradiance distribution

Figure 2 shows that a Gaussian beam is incident on an Axicon lens that transforms the incident beam into an annular beam, and a biconvex lens transforms the annular beam into a collimated outer half-Gaussian hollow beam [8] as shown at the plane AB. The outer radius and thickness of this hollow beam, $R_{out}$ and $R_0$ respectively, can be expressed as $R_{out} = L \cdot \tan(\beta - \alpha)$ and $R_0 = R_G[1 - \tan\alpha \cdot \tan(\beta - \alpha)]$.,

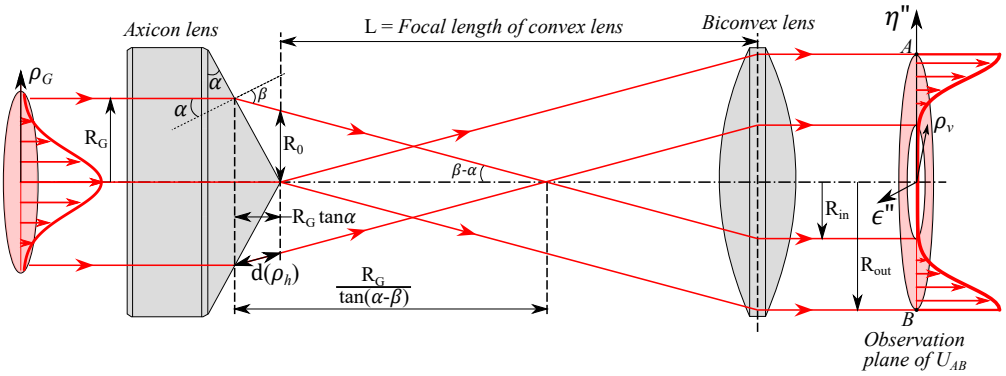


**Fig. 2.** Laser propagation path for determining geometrical features of the beam.

where $L$ is the distance between the axicon and biconvex lenses, $\alpha$ and $\beta$ are the angles of incidence and refraction at conical surface of the axicon lens as depicted in Fig. 2, and $\sin\beta = n \cdot \sin\alpha$ th $n$ being the refractive index of the lens material which is ZnSe in this study. The inner radius of the hollow beam, $R_{in}$, is now obtained as $R_{in} = R_{out} - R_0$.

The irradiance of the outer half-Gaussian beam is given by the following expression:

$$I(\rho_v) = I_0 e^{-\frac{2(\rho_v - R_{out})^2}{R_0^2}}. \tag{1}$$

where $\rho_v$ is the radial distance in polar coordinates for any points on the vertical cross section of the hollow beam with $\rho_v$ varying from $R_{in}$ to $R_{out}$. $\rho_v$ is given by $\rho_v(\epsilon'', \eta'') = \sqrt{\epsilon''^2 + \eta''^2}$ th $\epsilon''$ as the horizontal axis pointing outward from the plane of paper and $\eta''$ as the vertical axis in Cartesian coordinates as shown in Fig. 2. $I_0$ is the maximum irradiance that can be related to the laser power by the following expression:

$$I_0 = \frac{2P}{\pi R_0^2 \left[ e^{-\frac{2R_{out}^2}{R_0^2}} - 1 + \sqrt{2\pi}\frac{R_{out}}{R_0}\mathrm{erf}\left(\sqrt{2}\frac{R_{out}}{R_0}\right)\right]} \tag{2}$$

Optics EXPRESS

Considering the phase delay due to the axicon lens, the phasor of the outer half-Gaussian beam at the plane AB can be written as follows:

$$U_{AB}(\epsilon'', \eta'') = \sqrt{I_0} e^{-\frac{(\rho_v(\epsilon'', \eta'') - R_{out})^2}{R_0^2} + ikd(\rho_v(\epsilon'', \eta''))} \tag{3}$$

where $i$ is the imaginary unit. $k = 2\pi/\lambda$ is the wave number with $\lambda$ as the wavelength of the laser, and $d(\rho_v) = \frac{\cos\beta}{\sin\alpha}(R_{out} - \rho_v)$ represents the distance (or path length difference) along the direction of the laser beam propagation between the inclined surface of the axicon lens and the vertical plane at the tip of the axicon lens [29].

The hollow parabolic mirror of focal length $f$ reflects and focuses the incident outer-half-Gaussian hollow beam. The phasor of this reflected beam is given by the following Rayleigh-Sommerfeld diffraction formula [30]:

$$U_{OP}(P_0) = \frac{1}{i\lambda} \iint U_{PM}(P_1) \cdot \frac{e^{ikR}}{R} \cos\langle \hat{n}, \hat{r}_R \rangle \; dS \tag{4}$$

$U_{OP}(P_0)$ and $U_{PM}(P_1)$ are the phasors at an arbitrary point $P_0$ of coordinates (x,y,z) and another arbitrary point $P_1$ on the observation plane and the parabolic mirror, respectively, as shown in Fig. 3(a). $R$ is the distance between $P_1$ and $P_0$, $\hat{n}$ and $\hat{r}_R$ are the unit vectors normal to the mirror surface at point $P_1$ and along the straight line $P_1P_0$ respectively, and $dS$ is the infinitesimal area on the mirror surface. The domain of the double integration in Eq. (4) is the curved surface of the mirror and the evaluation of the integrals in this domain is complicated. To simplify the procedure, the domain of integration is transformed to a horizontal plane by expressing all variables in terms of the coordinates of the horizontal plane (Fig. 3(a)). The unit normal vector is, therefore, expressed as $\hat{n} = \hat{e}_z \cos\theta_p + \hat{e}_\eta \sin\theta_p$, where $\theta_p$ is the projection angle between the tangential plane of the parabolic mirror at $P_1$ and the horizontal plane, and $\hat{e}_z$ and $\hat{e}_\eta$ are the unit vectors in the $z$ and $\eta$ directions in Cartesian coordinates. $dS$ is, similarly, expressed as $dS = \frac{dA}{\cos\theta_p}$ where $dA$ is an infinitesimal area on the horizontal plane.

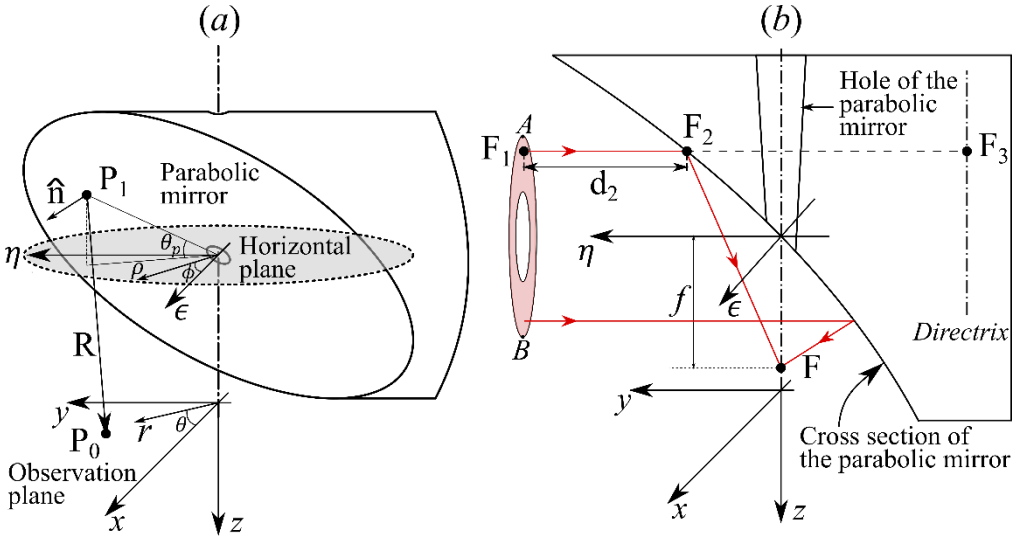


**Fig. 3.** Coordinate systems used in the Rayleigh-Sommerfeld diffraction formula for calculating the distance from the points on the parabolic mirror to the points on the plane of observation.

Setting the origin of the Cartesian coordinates $(\epsilon, \eta, z)$ at the center of the hole on the parabolic mirror, the coordinates of $P_1$ can be expressed in terms of $(\epsilon, \eta, \mp\xi)$ with $\xi = \sqrt{\epsilon^2 + \eta^2} \cdot \tan\theta_p$ and,

Optics EXPRESS

therefore, $U_{PM}(P_1) \equiv U_{PM}(\epsilon, \eta, \bar{+}\xi)$. Here the negative and positive signs are for the points $P_1$ located above and below the horizontal plane (Fig. 3(a)), respectively, since the z axis is negative above the horizontal plane. Therefore, the distance vector between the light source point $P_1$ and the observation point $P_0$ is $\vec{R} = \overrightarrow{P_1P_0} = (x-\epsilon)\hat{e}_x + (y-\eta)\hat{e}_y + (z \pm \xi)\hat{e}_z$, the unit vector along $\vec{R}$ is $\hat{r}_R = \frac{(x-\epsilon)\hat{e}_x+(y-\eta)\hat{e}_y+(z\pm\xi)\hat{e}_z}{\sqrt{(x-\epsilon)^2+(y-\eta)^2+(z\pm\xi)^2}}$, and the magnitude of $\vec{R}$ is $R = \sqrt{(x-\epsilon)^2 + (y-\eta)^2 + (z \pm \xi)^2}$. So the inclination factor in Eq. (4) can be written as $\cos\langle \hat{n}, \hat{r}_R \rangle = \hat{n} \cdot \hat{r}_R = \frac{(y-\eta)\sin a+(z\pm\xi)\cos\theta_p}{(z\pm\xi)\left[1+\left(\frac{x-\epsilon}{z\pm\xi}\right)^2+\left(\frac{y-\eta}{z\pm\xi}\right)^2\right]}$.

The distance between the source plane ($\epsilon\eta$) and the observation plane (xy) is generally large compared to the distances in the x and y directions, especially, when the laser is focused onto the neighborhood of the origin of the x and y axes. Under this condition, the Fresnel approximation [30] can be applied and the inclination factor becomes $\cos\langle \hat{n}, \hat{r}_R \rangle \approx \cos\theta_p$ in this study.

The phasor $U_{PM}(P_1)$ in Eq. (4), i.e., $U_{PM}(\epsilon, \eta, \bar{+}\xi)$, can be determined by introducing a phase factor to Eq. (3) and applying coordinate transformation to $\rho_v(\epsilon'', \eta'')$. This additional phase corresponds to the optical path length traveled by the light from the plane AB to the surface of the parabolic mirror (Figs. 2 and 3(b)). The plane AB of Fig. 2 is included in Fig. 3(b) for clarity and two typical paths of the light are shown to highlight the phase delay distance, e.g., $F_1F_2 = d_2$, from the plane AB to the point of incidence on the mirror. Also shown in Fig. 3(b), the paths of the light reflected off the mirror toward a horizontal focal plane at the point F. The annular laser spot is oriented vertically at the plane AB with coordinates $(\epsilon'', \eta'')$ for various points on the spot. When the light from this spot is incident on the mirror at an angle of incidence $\theta_{im}$, a slanted annular laser spot is formed with a certain curvature conforming to the shape of the mirror surface. The points on this slanted and curved annular spot can be described by the coordinates $(\epsilon', \eta', \zeta')$ with the origin at the center of the hole of the mirror. The plane $\epsilon'\eta'$ is tangential to the curved mirror surface at the center of the hole and $\zeta'$ represents the variation of the curved surface relative to this tangential plane. To simplify the integration in Eq. (3) as discussed earlier, the slanted and curved annular spot is projected further onto a horizontal $\epsilon\eta$ plane.

The projection angle $\theta_p$ depends on the position of point $P_1$ due to the curvature of the parabolic mirror. The effect of curvature is neglected in this study for large focal lengths of the parabolic mirror, resulting in a slanted planar annular spot on the mirror surface, and therefore the projection angle $\theta_p$ can be considered constant. Under this approximation, the projection of the slanted annular beam onto the horizontal ($\epsilon\eta$) plane will have the same shape as the vertically oriented annular spot with the same inner and outer radii $R_{in}$ and $R_{out}$, respectively, when $\theta_{im} = \pi/4$. For an arbitrary value of $\theta_{im}$, the coordinate transformation from the vertical plane AB to the slanted planar plane and then to the horizontal $\epsilon\eta$ plane can be represented by $(\epsilon'', \eta'') \rightarrow (\epsilon',') \rightarrow (\epsilon, \eta)$, which yields $\rho_v(\epsilon'', \eta'') = \sqrt{\epsilon'2 + \eta''2} = \sqrt{\epsilon'2 + \eta'2\cos^2\theta_{im}} = \sqrt{\epsilon^2 + \eta^2\cot^2\theta_{im}} = \rho_h(\epsilon, \eta)$ with $\rho_h$ transforming the radial distance $\rho_v$ from the vertical plane to the horizontal plane. Now the phasor $U_{PM}$ can be written as follows by modifying Eq. (3) with a phase factor due to the phase delay distance $d_2$:

$$U_{PM}(\epsilon, \eta, \bar{+}\xi) = \sqrt{I_0}e^{-\frac{[\rho_h(\epsilon,\eta)-R_{out}]^2}{R_0^2}+ik(d(\rho_h(\epsilon,\eta))+d_2(\epsilon,\eta,\bar{+}\xi))} \tag{5}$$

$d_2$ can be determined by noting that the perpendicular distance from a point on a parabola to its directrix ($F_2F_3$ in Fig. 3(b)) is equal to the distance from that point on the parabola to its focus ($F_2F$), i.e., $F_2F_3 = F_2F$. Since the plane AB is parallel to the directrix plane, the distance between these two planes would be the same for any point on the plane AB, i.e., $F_1F_3 = C$ where C is a constant. So the phase delay distance $d_2 = F_1F_2 = F_1F_3 - F_2F_3 = C - F_2F_3 = C - F_2F$. The coordinates of $F_2$ and F are $(\epsilon, \eta, \bar{+}\xi)$ and (0,0,$f$), respectively, where $f$ is the focal length of the parabolic mirror, which yields $F_2F = \sqrt{\epsilon^2 + \eta^2 + (f \pm \xi)^2} = \sqrt{\epsilon^2 + \eta^2 + \left(f \pm \sqrt{\epsilon^2 + \eta^2}\tan\theta_p\right)^2} = \sqrt{\rho^2 + (f \pm \rho\tan\theta_p)^2}$,

Optics EXPRESS

where $\rho = \sqrt{\epsilon^2 + \eta^2}$. Since the constant C introduces the same phase change for all the light paths, the effect of C can be neglected and, therefore, the expression for $d_2 = -F_2F = -\sqrt{\rho^2 + (f \pm \rho \tan\theta_p)^2}$ is applied to Eq. (5).

Now the phasor at the point $P_0(x, y, z)$ can be calculated by applying Eq. (5) to the Rayleigh-Sommerfeld formula as given in Eq. (4):

$$U_{OP}(P_0) = U(x, y, z) = \frac{1}{i\lambda}\iint U_{PM}(\epsilon, \eta, \mp\xi) \cdot \frac{e^{ikR}}{R} \cos\left\langle \vec{n}, \overrightarrow{r_R} \right\rangle \frac{dA}{\cos\theta_p} = \frac{1}{i\lambda}\iint U_{PM} \cdot \frac{e^{ikR}}{R}\, dA \tag{6}$$

The following expression is obtained from Eq. (6) after applying the Fresnel approximation:

$$U(x, y, z) = \frac{\sqrt{I_0}e^{ik(z\pm\xi)}}{i\lambda(z \pm \xi)} \iint e^{-\frac{(\rho_h - R_{out})^2}{R_0^2}} e^{ik\left[d + d_2 + \frac{(x-\epsilon)^2}{2(z\pm\xi)} + \frac{(y-\eta)^2}{2(z\pm\xi)}\right]} dA \tag{7}$$

Changing the variables of integration from the Cartesian coordinates to polar coordinates, i.e., $\epsilon = \rho\cos\phi,\ \eta = \rho\sin\phi; x = r\cos\theta,\ y = r\sin\theta$, Eq. (7) can be written as follows for the case of $\theta_{im} = \pi/4$:

$$\begin{aligned} U(r, \theta, z) = {} & \frac{\sqrt{I_0}}{i\lambda} \int_{\rho=R_{in}}^{R_{out}} \frac{e^{ik(z+\xi)}}{z + \xi} \int_{\phi=0}^{\pi} e^{-\frac{(\rho - R_{out})^2}{R_0^2}} e^{ik(d+d_2)} e^{\frac{ik(r^2+\rho^2)}{2(z+\xi)}} e^{-\frac{ik r\rho}{z+\xi}\cos(\phi-\theta)}\, \rho d\phi d\rho + \\ & \frac{\sqrt{I_0}}{i\lambda} \int_{\rho=R_{in}}^{R_{out}} \frac{e^{ik(z-\xi)}}{z - \xi} \int_{\phi=\pi}^{2\pi} e^{-\frac{(\rho - R_{out})^2}{R_0^2}} e^{ik(d+d_2)} e^{\frac{ik(r^2+\rho^2)}{2(z-\xi)}} e^{-\frac{ik r\rho}{z-\xi}\cos(\phi-\theta)}\, \rho d\phi d\rho \end{aligned} \tag{8}$$

The integral with respect to $\phi$ can be evaluated using the integral representation of the zeroth-order Bessel function of the first kind, i.e., $J_0(x) = \frac{1}{\pi}\int_0^{\pi} e^{-ix\cos(\phi-\theta)} d\phi$, and applying the Fresnel aroximation to $\xi$, i.e., $\xi = \rho\tan\theta_p \ll z$, to simplify Eq. (8) as:

$$U(r, z) = -\frac{i2\pi\sqrt{I_0}}{\lambda z} e^{ik\left(\frac{r^2}{2z} + z - f\right)} \int_{\rho=R_{in}}^{R_{out}} e^{-\frac{(\rho - R_{out})^2}{R_0^2}} e^{ik\left[(R_{out} - \rho)\frac{\cos\beta}{\sin\alpha} + \frac{\rho^2}{2z}\right]} J_0\left(\frac{kr\rho}{z}\right)\, \rho d\rho \tag{9}$$

Rewriting the integral in the following form,

$$F(r, z) = \int_{\rho=R_{in}}^{R_{out}} \exp\left[\left(-\frac{1}{R_0^2} + i\frac{k}{2z}\right)\rho^2 + \left(\frac{2R_{out}}{R_0^2} - ik\frac{\cos\beta}{\sin\alpha}\right)\rho + \left(-\frac{R_{out}^2}{R_0^2} + ik\frac{\cos\beta}{\sin\alpha}R_{out}\right)\right] J_0\left(\frac{kr\rho}{z}\right)\, \rho d\rho \tag{10}$$

and integrating Eq. (10) by parts 3 times, an approximate expression is obtained for $F(r, z)$:

$$F(r, z) \approx e^{aR_{out}^2 + bR_{out} + c} \cdot \frac{zR_{out}}{kr}\, J_1\left(\frac{kr}{z}R_{out}\right) - e^{aR_{in}^2 + bR_{in} + c} \cdot \frac{zR_{in}}{kr}\, J_1\left(\frac{kr}{z}R_{in}\right) \tag{11}$$

where $a = -\frac{1}{R_0^2} + i\frac{k}{2z}$, $b = \frac{2R_{out}}{R_0^2} - ik\frac{\cos\beta}{\sin\alpha}$, and $c = -\frac{R_{out}^2}{R_0^2} + ik\frac{\cos\beta}{\sin\alpha}R_{out}$. Applying Eq. (11) to Eq. (9), the phasor on the xy plane is found to be:

$$U(r, z) = -\frac{\sqrt{I_0}}{r} e^{i\frac{\pi}{2}} e^{ik\left(\frac{r^2}{2z} + z - f\right)} \left[e^{ik\frac{R_{out}^2}{2z}} R_{out}\, J_1\left(\frac{kR_{out}}{z}r\right) - e^{-2 + ik\left(\frac{R_0\cos\beta}{\sin\alpha} + \frac{R_{in}^2}{2z}\right)} R_{in}\, J_1\left(\frac{kR_{in}}{z}r\right)\right] \tag{12}$$

and the corresponding irradiance distribution is:

$$\begin{aligned} I(r, z) = {} & \frac{I_0}{r^2}\left[R_{out}^2\, J_1^2\left(\frac{kR_{out}r}{z}\right) + R_{in}^2\, J_1^2\left(\frac{kR_{in}r}{z}\right) e^{-4}\right. \\ & \left. -2R_{in}R_{out}J_1\left(\frac{kR_{in}r}{z}\right) J_1\left(\frac{kR_{out}r}{z}\right) \cos\left(\frac{R_{out}^2 - R_{in}^2}{2z} - \frac{R_0\cos\beta}{\sin\alpha}\right) e^{-2}\right] \end{aligned} \tag{13}$$

Optics EXPRESS

Equation (13) influences the heat flux on the substrate surface and thus affect the temperature distribution in the material.

### 3.2. Bessel-Gaussian laser heating of moving substrates

A portion of the laser beam is reflected, and the rest of the energy is absorbed at the substrate surface when the transmittance of the substrate is zero. The absorbed energy manifests as heat flux on the surface of the substrate and provides the thermal energy for evaporating the liquid of the nanoparticle suspension and sintering the nanoparticles to deposit a thin film on the substrate surface. The irradiance of the BG beam is used to determine the heat flux as a boundary condition in the following heat conduction model. This model is applied to the case of depositing Ag lines on a moving ITO-coated Si substrate using an Ag ink. The temperature distribution of the model is used for selecting the laser processing parameters to heat without any thermal damage to the Si substrate and also predict the width of the deposited Ag lines.

Shown in Fig. 4 is the schematic of the conduction model in the Cartesian coordinates with the heat flux due to laser irradiation at the top surface of the substrate. The Ag ink is delivered to the right side of the laser spot and this unsintered ink passes through the spot as the substrate moves in the negative $x$ direction with velocity $V$, resulting in the sintered Ag line on the left side of the spot. The effects of heating the Ag ink and the substrate motion are considered in the boundary condition for the heat flux at the top (z = H) surface of the substrate as discussed later in this section. The effect of ITO, however, is neglected since it is very thin (1–3 $\mu m$). Therefore, the governing equation for the temperature distribution, T(x,y,z,t), in the Si substrate can be written as follows by considering temperature-dependent thermophysical properties:

$$\frac{\partial}{\partial x}\left(k(T)\frac{\partial T}{\partial x}\right)+\frac{\partial}{\partial y}\left(k(T)\frac{\partial T}{\partial y}\right)+\frac{\partial}{\partial z}\left(k(T)\frac{\partial T}{\partial z}\right)=\frac{k(T)}{\alpha}\frac{\partial T}{\partial t} \tag{14a}$$

where $k(T)$ and $\alpha$ are the thermal conductivity and thermal diffusivity of silicon respectively. The thermal diffusivity is generally a slowly varying function of T and, therefore, it is considered constant in this study. The heat flux boundary conditions are applied to all the surfaces by considering both convection and radiation heat losses to the ambient air. The boundary condition at the top (z = H) surface, however, contains an additional term that represents the absorbed energy flux due to the incident laser irradiance. The absorbance of silicon wafers at the wavelength of a $CO_2$ laser is nearly zero. The substrate surrounding the Ag line is heated up due to heat conduction from the Ag lines during the sintering process. Therefore, the silicon substrate is expected to lose heat to the ambient air due to both convection and radiation mechanisms. These two mechanisms have been considered in the boundary conditions (14b-g). Also the total convection heat transfer coefficient, $h_t$, at the top surface is the sum of the convection heat transfer coefficient to the ambient air, $h_4$, and another heat transfer coefficient, $h_{Ag}$, pertaining to the loss of energy for heating the Ag film, i.e., $h_t = h_4 + h_{Ag}$. The initial condition for solving Eq. (15a) is taken as the ambient temperature, $T_a$, by considering that the substrate is initially at room temperature. These boundary and initial conditions can be expressed as:

$$k(T)\frac{\partial T}{\partial x}=h_1(T-T_a)+\sigma\tilde{\epsilon}_{Si}(T^4-T_a^4) \qquad at \qquad x=0 \tag{14b}$$

$$-k(T)\frac{\partial T}{\partial x}=h_1(T-T_a)+\sigma\tilde{\epsilon}_{Si}(T^4-T_a^4) \qquad at \qquad x=L \tag{14c}$$

$$k(T)\frac{\partial T}{\partial y}=h_2(T-T_a)+\sigma\tilde{\epsilon}_{Si}(T^4-T_a^4) \qquad at \qquad y=0 \tag{14d}$$

$$-k(T)\frac{\partial T}{\partial y}=h_2(T-T_a)+\sigma\tilde{\epsilon}_{Si}(T^4-T_a^4) \qquad at \qquad y=W \tag{14e}$$

Optics EXPRESS

$$k(T)\frac{\partial T}{\partial z} = h_3(T - T_a) + \sigma\tilde{\epsilon}_{Si}(T^4 - T_a^4) \qquad at \qquad z = 0 \tag{14f}$$

$$k(T)\frac{\partial T}{\partial z} = \frac{A_{Ag}}{A_{LS}} I_h(x, y, t)(1 - R_{Ag}) - h_t(T - T_a) - \sigma\bar{\epsilon}(T^4 - T_a^4) \qquad at \qquad z = H \tag{14g}$$

$$T(x, y, z) = T_a \qquad at \qquad t = 0 \tag{14h}$$

where $L$, $W$ and $H$ are the length, width and height respectively (Fig. 4). $h_i$ represents the convection heat transfer coefficient at the substrate surfaces for i = 1,2,3,4. $\sigma$ and $\tilde{\epsilon}_{Si}$ are the Stefan-Boltzmann constant and thermal emissivity of the substrate respectively. $\bar{\epsilon}$ is an average thermal emissivity based on the properties of silicon and silver. $I_h(x, y, t)$ represents the moving heat flux due to the motion of the laser beam relative to the substrate and $R_{Ag}$ is the reflectance of silver at the $CO_2$ laser wavelength of 10.6$\mu$m. Noting that the velocity of the laser beam with respect to the substrate is $V$ in the x direction since the substrate moves in the negative x direction, the moving heat flux is related to the laser irradiance of Eq. (13) by the expression $I_h(x, y, t) = I\left(r = \sqrt{(x - Vt)^2 + y^2}, z = f\right)$.

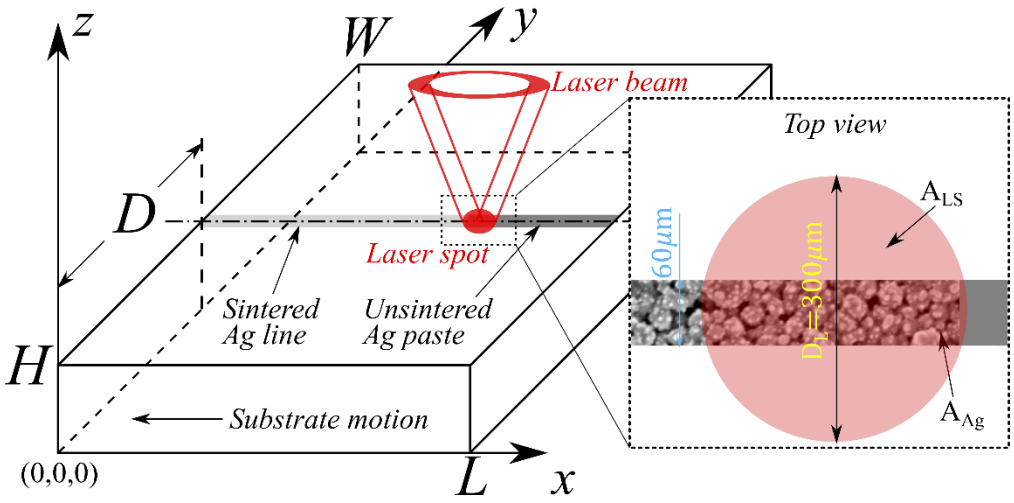


**Fig. 4.** Heat flux due to laser irradiation and the Cartesian coordinate system used in heat conduction model.

The energy of a quantum of the $CO_2$ laser is much lower than the bandgap energy of the Si substrate and, therefore, the substrate does not absorb the laser energy. The laser beam is absorbed by the Ag ink and the Ag nanoparticles during the sintering process and this mechanism is incorporated in the model by considering the reflectance of silver in the boundary condition (14g). In this study, however, the width of the Ag line is much smaller than the diameter of the laser spot as illustrated in Fig. 4 and, therefore, only a small area of the incident laser spot is utilized for heating the Ag line and substrate. Denoting the area of the Ag line by $A_{Ag}$ which is illuminated by the laser beam and the area of the entire laser spot by $A_{LS}$, the power contained in $A_{Ag}$ would be $P{\cdot}A_{Ag}/A_{LS}$. Since P is included in the term $I_h(x,y,t)$, the line illumination factor, $A_{Ag}/A_{LS}$, is introduced in the boundary condition (14g). The area of the Ag line is estimated by considering the volumetric flow rate at which the Ag ink is delivered to the substrate and the speed of the substrate, resulting in $A_{Ag} \approx 0.0153\text{mm}^2$, where the spreading of the ink on the substrate surface due to surface tension and the viscous resistance to the spreading are neglected. The heat conducts from the Ag line into the Si substrate, resulting in a hot Si surface adjacent to

Optics EXPRESS

the line and, therefore, an area average emissivity, $\bar{\epsilon} = 0.216\tilde{\epsilon}_{Ag} + 0.784\tilde{\epsilon}_{Si}$, is considered in this study, where $\tilde{\epsilon}_{Ag}$ and $\tilde{\epsilon}_{Si}$ are the emissivities of Ag and Si respectively.

The thermal conductivity data [31] of Si are expressed as a function of temperature, $k(T) = p \cdot T^q$ with p = $10^{5.75}$ and q = -1.41 in the temperature range 300K to 1000K, and an average value of the thermal diffusivity is taken as $\alpha = 0.8\text{cm}^2/\text{s}$. The emissivities of Ag and Si are [32,33] $\tilde{\epsilon}_{Ag} = 0.793$ and $\tilde{\epsilon}_{Si} = 0.67$, and the reflectance of Ag is $R_{Ag} = 0.98$. In our experimental set up, the convection heat transfer to the ambient air is due to natural convection. The heat transfer coefficient varies from 2 to 25W/($m^2$·K) for natural convection [34]. An intermediate value of 10W/($m^2$·K) has been chosen for $h_i$, i= 1,2,3,4, in this study. $h_{Ag}$ is estimated by considering the effect of the coated silver ink as an additional heat convection coefficient, i.e., $h_{Ag} = \frac{\rho_{Ag} C_{p,Ag} H_{Ag} V}{L}$, where $\rho_{Ag}$, $C_{p,Ag}$ and $H_{Ag}$ are the density, specific heat capacity and height of the Ag film deposited on the substrate surface. The derivation of $h_{Ag}$ is presented in Appendix A.

Equation (14a) is a nonlinear heat conduction problem which Kar et al. [35] solved by linearizing the problem using the Kirchhoff transform and then applying the finite-medium Fourier transform in the x, y and z directions. They determined the temperature distribution in stainless steel substrates for the case of laser heating with a Gaussian beam. In their study, the irradiance profile was a Gaussian function that exhibits a monotonically decreasing profile with a maximum irradiance at the center of the beam and very low irradiance at the edge of the beam. In the present study, however, the irradiance profile involves the Gaussian and Bessel functions, exhibiting an oscillatory profile with a principal maximum irradiance at the center of the beam and rings of subsidiary maximum irradiances surrounding the principal maximum. The effect of this Bessel-Gaussian beam on the temperature distribution is analyzed in this paper by following Kar et al.'s method [35]. The solution of the above thermal model, Eq. (14a) and boundary and initial conditions (14b-h), is summarized by the following temperature distribution:

$$T = T_0 \cdot [1 + (q+1)T'^*]^{-(q+1)} \tag{15}$$

where $T_0$ is a reference temperature which is taken as 373K in this study, and

$$T'^* = -T_c^* + \sum_{l=0}^{\infty} \frac{X(x^*)}{N_{lx}} \sum_{m=0}^{\infty} \frac{Y(y^*)}{N_{my}} \times$$

$$\left[\bar{\Theta}_2 + \sum_{n=0}^{\infty} \frac{Z(z^*)}{N_{nz}} \left(\tilde{\Theta}_i e^{-\lambda_{lmn}^2 t^*} - \tilde{\Theta}_2 + e^{-\lambda_{lmn}^2 t^*} \int_0^{t^*} Fo \cdot \lambda_{nz}^2 \cdot s^{*2} \tilde{\Theta}_2(\tau) e^{\lambda_{lmn}^2 \tau}\, d\tau\right)\right] \tag{16}$$

Here the dimensionless spatial and temporal variables are defined as $x^* = \frac{x}{L}$, $y^* = \frac{y}{W}$, $z^* = \frac{z}{H}$ and $t^* = \frac{Vt}{L}$. The eigenvectors $X(x^*)$, $Y(y^*)$ and $Z(z^*)$, eigenvalues $\lambda_{lx}$, $\lambda_{my}$ and $\lambda_{nz}$, and normalization constants $N_{lx}$, $N_{my}$ and $N_{nz}$ in the x, y and z directions, respectively, are presented in Appendices B and C. These two appendices also provide the expressions for the other variables that appear in Eq. (16) and various integrals involving the BG irradiance profiles. Equation (16) is used to obtain the isotherms for determining the width of the sintered Ag films and to examine the effect of various laser processing parameters on the temperature of the substrate.

## 4. Results and discussion

### 4.1. Model validation

Isotherms are plotted in Fig. 5 to show the temperature contours both on the top surface and along the thickness of the substrate for the case of incident laser power 11.8W, substrate speed 1mm/s, and Ag ink feed rate of 100nL/min with a capillary tube of inner diameter (ID) 51μm. The isotherms on the top surface are utilized to predict the width of the sintered Ag line by considering that the sintering occurs only above a certain threshold temperature. The threshold is set to be $180 \circ C$ in this study since this temperature is within the range of the silver ink curing

Optics EXPRESS

temperatures [26,27]. Applying this criterion to Fig. 5, the predicted Ag line width is found to be 64$\mu m$ for nanoparticle dispensing capillary tube of ID 51μm. The thermal model was applied to another case with the same sintering condition as above except for a different capillary tube of ID 108μm, and the predicted Ag line width was found to be 122$\mu m$.

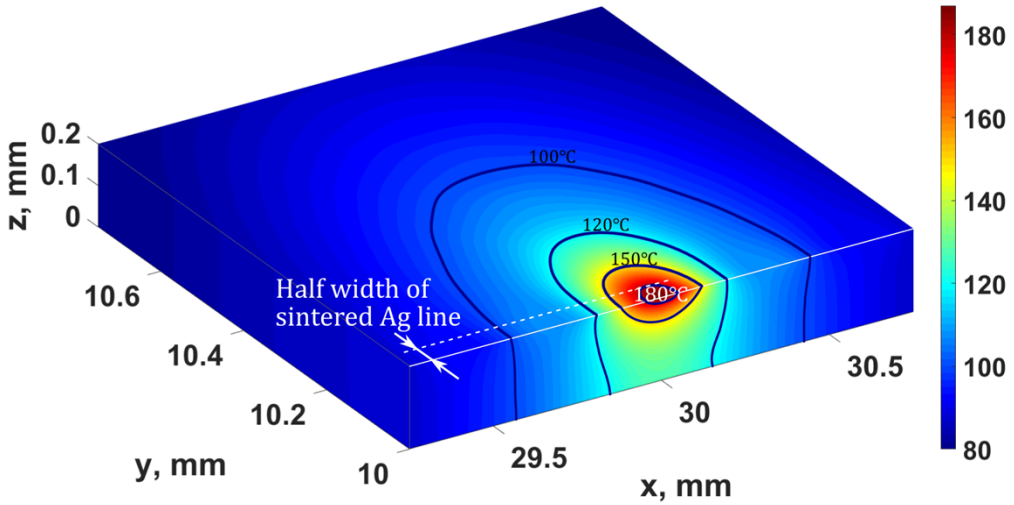


**Fig. 5.** Temperature distribution in silicon substrate during Ag line deposition. Zoomed in view of the isotherms, showing the sintering threshold isotherm of 180 ∘ $C$ for predicting the Ag line width. Process parameters for temperature calculation: $Q$ = 100nL/min, ID = 51μm, $H_{ct}$ = 50$\mu m$, $\theta_{in}$ = 40°, P = 11.8W, $V$ = 1$mm/s$, $d_{ct}$ = 1.5$mm$ and $D_L$ = 300$\mu m$.

To validate the model predictions, experiments were conducted using the apparatus shown in Fig. 1 for sintering Ag nanoparticles to deposit Ag films as a narrow line on a Si substrate. For the above-mentioned two cases of tube ID 51 μm and 108 μm, the experimental line widths (Fig. 6) range from 59 to 62$\mu m$ and 117 to 122$\mu m$, respectively, which agree with the predicted line widths fairly well. The widths were measured at different locations along the length of the line due to the nonuniformity in the width. The average line width and thickness are 60μm and 1.11μm, respectively, for the case of 51$\mu$m ID tube and 120μm and 1μm, respectively, for the larger tube of 108$\mu$m ID under the same drying and sintering conditions as for the smaller tube. Figure 6 shows optical microscopic and Secondary Electron Microscopic (SEM) images, and Electron Dispersive X-ray (EDX) data for the composition of various elements in the sintered Ag film. The optical micrographs of the Ag lines show that the widths vary slightly along the length of the lines and the SEM images exhibit nanosize clusters formed by the sintered Ag nanoparticles. The EDX spectrographs, on the other hand, demonstrate the purity of the process for depositing contaminant-free Ag lines, even though the process was carried out in an open space with ambient air. Dominant Ag peaks can be seen in both Figs. 6(a) and 6(b) with extremely small peaks of C atoms, indicating that the organic liquid of the Ag nanosuspension is almost completely evaporated. While no peaks of $O_2$ and Si atoms exist in Fig. 6(a), there presence in Fig. 6(b) may be due to the native oxide of Si in the original Si substrate. The presence of S peak is ascribed to contamination during cleaning and handling of the samples after the deposition process.

The model was also used to examine the effect of laser power on the sintered Ag line width as shown in Fig. 7. It includes the experimental line widths as well for comparison between the experimental data and theoretical predictions. When the experiments were run at the laser power 8.9 W, no deposition of Ag film occurred which is also predicted by the model. Although

Optics EXPRESS

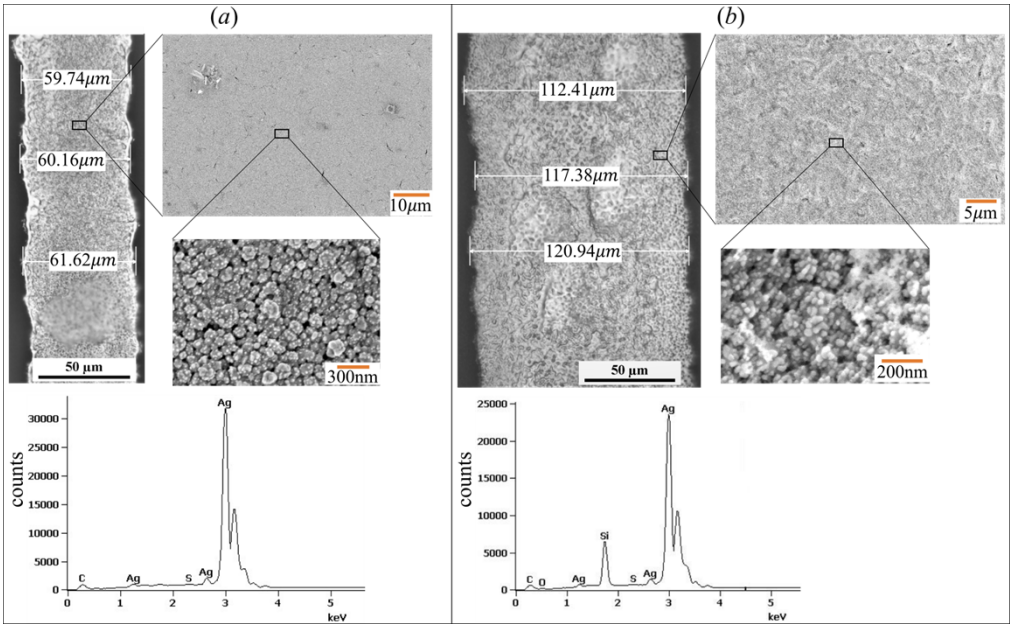


**Fig. 6.** Deposited silver lines on ITO-coated substrate. Optical microscopic and SEM images, and EDX data for a silver line deposited with a capillary tube of inner diameter (a) 51 $\mu$m and (b) 108 $\mu$m. Process parameters for deposition: $Q = 100$nL/min, ID = 51μm, $H_{ct} = 50\mu m$, $\theta_{in} = 40°$, P = 11.8W, $V = 1mm/s$, $d_{ct} = 1.5mm$ and $D_L = 300\mu m$.

the Ag lines were deposited at 11.8 W in this study, Fig. 7 shows that lines of smaller width can be deposited below 11.8W but above certain threshold powers. Also Fig. 7 indicates that extremely narrow, e.g., a few micrometers or nanometers wide, Ag lines can be deposited with laser powers slightly above the threshold value. The threshold powers for sintering are 10.45 W and 11.3 W for capillary tubes of ID 108 μm and 51 μm, respectively. This change in the threshold power with tube ID is attributed to the variation in the width and thickness of the initial liquid (Ag ink) line produced on the substrate surface by different capillary tubes. A larger ID tube would produce wider and thinner liquid lines than a smaller ID tube under the same mass flow rate of the nanosuspension and the same substrate speed. and, correspondingly, fewer Ag nanoparticles would be present per unit volume of the liquid line in the case of nanosuspension dispensation with a larger tube. The laser is, therefore, required to heat less materials in thinner films to achieve the threshold sintering temperature which is taken as 180°C for Ag nanoparticles in this study. These two phenomena, the nanosuspension dispensation and the laser heating of fewer nanoparticles, influence the width and thickness of the final product which is formed after the initial liquid Ag line is sintered. The combined effect of these two phenomena may be the reason for lower threshold power in the case of larger ID tube. For the same laser power, e.g., 11.8 W, the larger ID tube yields wider and thinner sintered Ag line than in the case of the smaller ID tube as evident from the experimental data discussed earlier in this section.

For the same width of sintered Ag line, Fig. 7 shows that the larger ID tube requires lower laser power that the smaller tube. To produce the same width by both the tubes, the laser must heat the same width with a boundary of 180°C isotherm. Since a larger ID tube yields fewer nanoparticles per unit volume of the liquid line, lower power would be needed to create the required isotherm than in the case of a smaller ID tube. Figure 7 also shows that the larger ID tube produces wider Ag lines than the smaller ID tube for the same laser power. This result is due to the above-mentioned two phenomena as well. A larger ID tube produces wider Ag liquid

Optics EXPRESS

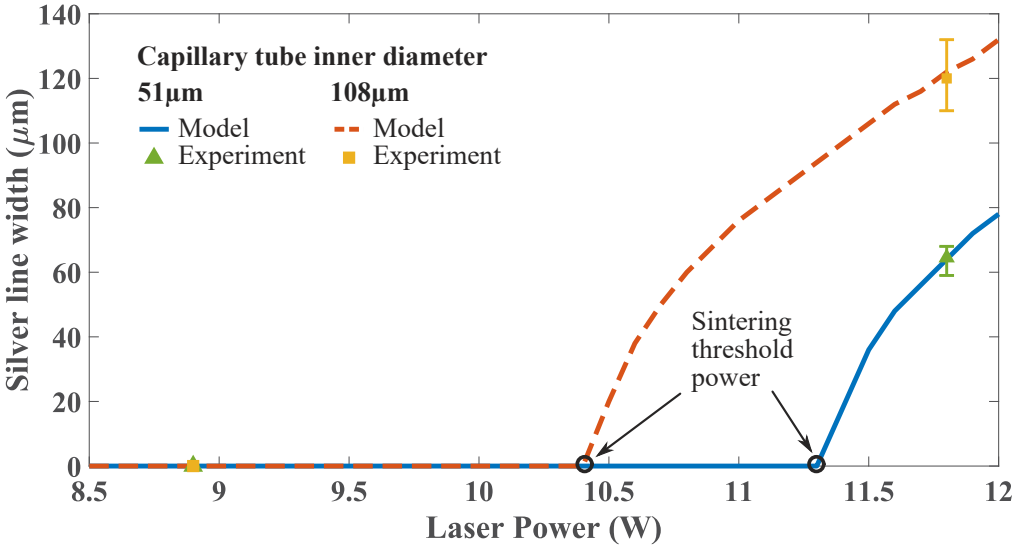


**Fig. 7.** Validation of thermal model for silver line deposition and prediction of threshold laser power for sintering. Process parameters for deposition: $Q = 100$nL/min, Capillary tube inner diameter = 51µm and 108µm, $H_{ct} = 50\mu m$, $\theta_{in} = 40°$, P = 11.8W, $V = 1mm/s$, $d_{ct} = 1.5mm$ and $D_L = 300\mu m$.

lines than a smaller ID tube and, consequently, the concentration of nanoparticles is lower in the former case. A given laser power, therefore, will be able to heat the nanoparticles above the threshold sintering temperature 180°C in a wider region in the case of a larger ID tube.

### 4.2. *Irradiance profile from the diffraction model*

The laser beam patterns change significantly as the beam passes through different lenses and the parabolic mirror. Shown in Fig. 8 are the laser irradiance distributions as a function of the beam radius at the exit of the $CO_2$ laser device, after the biconvex lens and at the focal plane of the parabolic mirror. The laser comes out of the laser device as a Gaussian beam of diameter 4.06mm. The Gaussian beam is transformed to a hollow beam after passing through the axicon and biconvex lenses and the irradiance profile in the ring of this beam is outer half-Gaussian as discussed in section 3.1. The hollow beam is then reflected and focused by the parabolic mirror, resulting in a Bessel-Gaussian irradiance pattern due to interference of the light arriving from various points of the ring to the substrate surface. This BG beam consists of a principal maximum irradiance at the center of the beam and subsidiary maxima at different points in the beam. The effect of the subsidiary irradiances on the temperature distribution is discussed in the next section.

### 4.3. *Parametric studies on laser heating and temperature distribution*

The temperature distribution in the silicon substrate is examined for different process parameters by considering the length (L), width (W) and height (H) of the substrate as $60mm$, $30mm$ *and* $0.2mm$, respectively. Two cases of laser heating are analyzed when the laser beam scans the top surface of the substrate, i.e., the laser beam moves relative to the substrate, in two different trajectories. In one case, the laser follows a symmetric track along the center line on the top surface and the trajectory is the locus of the coordinates (x, D, 0) for D = 15 mm and $0 \leq x \leq L$. In the second case, the laser follows an asymmetric track along an off-center line on the top surface and the trajectory is the locus of the coordinates (x, D, 0) for D = 10 mm and $0 \leq x \leq L$. The

Optics EXPRESS

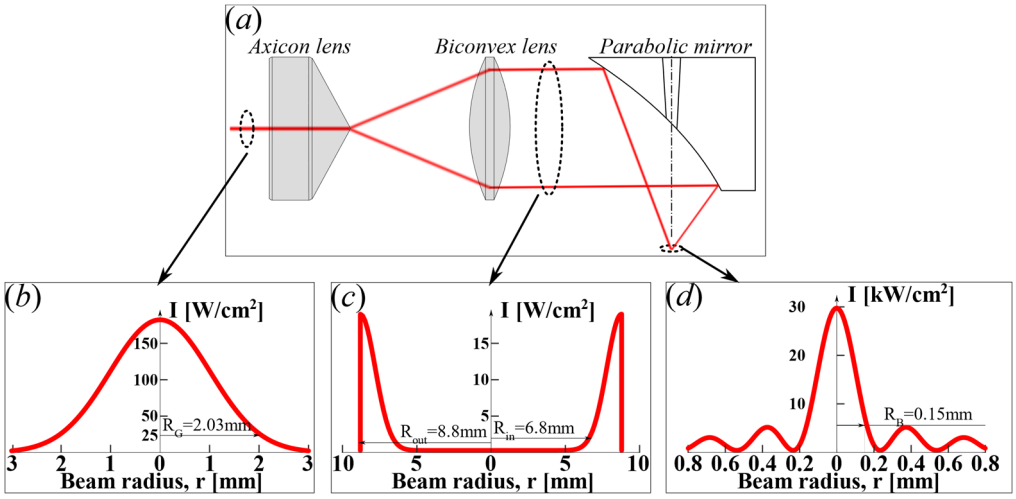


**Fig. 8.** Laser beam patterns at different locations of the laser path. (a) optical setup, (b) Incident Gaussian irradiance profile, (c) Outer half-Gaussian beam of inner and outer radii $R_{in} = 6.8mm$ and $R_{out} = 8.8mm$, respectively, and (d) Bessel-Gaussian beam with a principal maximum of radius $R_B = 0.15mm$.

dimensionless distances of the track from the front (y = 0) surface of the substrate are $D^* = 0.5$ and $D^* = 0.33$, where D* = D/W, for the symmetric and asymmetric tracks respectively. The laser power is set at 11.8W and the scanning speed at $V = 1$ mm/s for both cases.

Figures 9(a,b) and 9(c,d) show the isotherms on the top surface of the substrate for the asymmetric and symmetric cases, respectively. Two different times, t = 3 s and 36 s, are considered for each case, and these two times yield the locations of the laser beam center on the substrate surface at two different points (Vt, D) where the temperature is maximum. The temperature distribution is asymmetric for the case of $D^* = 0.33$, showing higher temperatures in the region between the laser track and the front (y = 0) surface of the substrate. This asymmetry is due to the slow convection and radiation heat losses, resulting in accumulated internal energy that raises the temperature. For the case of $D^* = 0.5$, on the other hand, the laser heating is a perfectly symmetric problem and, therefore, the temperature distribution is symmetric as shown in Figs. 9(c,d).

However, the temperature distribution in a small region of radius approximately 1.5 mm around the laser beam center is found to be symmetric regardless of the distance, D, of the scanning track from the y = 0 surface, since the effect of laser heating dominates over the convection and radiation heat losses in the neighborhood of the beam center. Figure 10(a) shows the temperature distribution along the laser scanning line on the top surface of the substrate when the beam center is at x = 30 mm and D = 10 mm, i.e., D* = 0.33, and Fig. 10(b) is the corresponding isotherm which exhibits symmetric temperature contour in the neighborhood of the beam center. Away from this neighborhood, however, the isotherms have convex or concave tips corresponding to the peaks or valleys of the temperature profile in Fig. 10(a). The BG irradiance profile of Fig. 8(d) is sketched on top of the temperature profile in Fig. 10(a) to illustrate that the peaks and valleys in the temperature profile correspond to the peaks and valleys in the BG beam profile. The wavy temperature profile is thus ascribed to the oscillatory irradiance profile.

It is also noticeable in Fig. 10 that the temperature contour is symmetric about the x = 30 mm and y = 10 mm lines over a small distance in these two directions. This symmetric feature generally occurs at low scanning speeds, such as 1 mm/s, since the conduction heat transfer is much faster than the advection mechanism at low speeds. The latter heat transfer mechanism

Optics EXPRESS

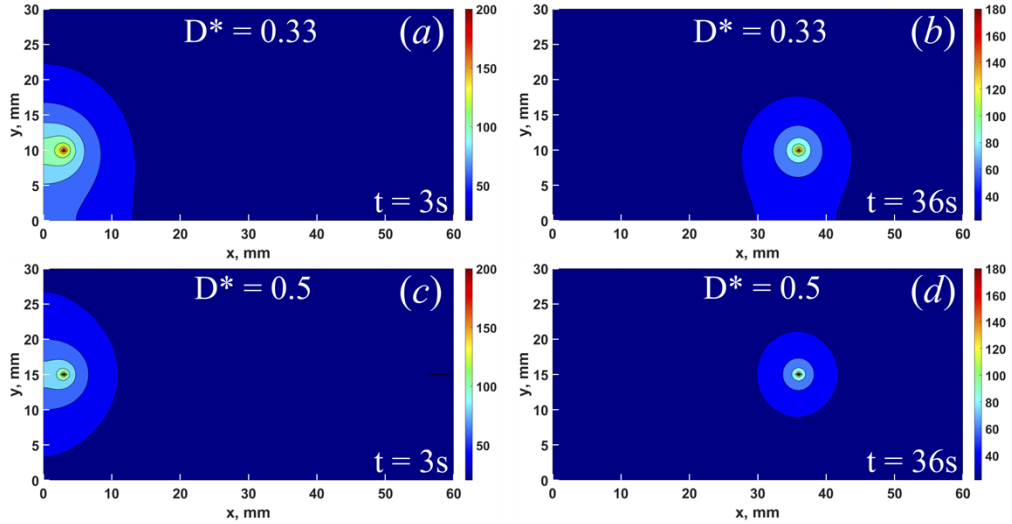


**Fig. 9.** Isotherms on the top surface of the substrate at selected positions of the moving laser beam center. (a, b) Asymmetric temperature contours at the points (3mm, 10mm) and (36mm, 10mm), and (c, d) Symmetric temperature contours at the points (3mm, 15mm) and (36mm, 10mm). Process parameters for temperature calculation: $Q = 100$nL/min, ID = 51µm, $H_{ct} = 50\mu m$, $\theta_{in} = 40°$, P = 11.8W, $V = 1mm/s$, $d_{ct} = 1.5mm$ and $D_L = 300\mu m$.

arises from the relative motion between the laser and the substrate. When the scanning speed is increased to $V = 40$mm/s, the effect of advection increases, resulting in lower temperatures in the leading edge than in the trailing edge of the beam as shown in Fig. 11(a). Similarly, the isotherms become densely spaced in the leading side than in the trailing side of the beam as in Fig. 11(b). Thus, the influence of advection compared to the conduction heat transfer induces an asymmetric temperature field along the laser scanning line. Considering the isotherm of 86°C in Fig. 11(b), the distance ($L_l$) of the leading edge of this isotherm is much shorter than the trailing edge ($L_t$) from the laser beam center. It can also be seen from the isotherms that the asymmetry occurs about the x = 30 mm line. It can also be seen that the temperature contours are still symmetric about the y = 10 mm line whereas they are asymmetric about the x = 30 mm line. This direction-dependent temperature field is caused by the direction of the laser beam scanning relative to the substrate. The laser scanning occurs only in the x direction relative to the substrate since the substrate is moved in the -x direction (Fig. 4) in this study, resulting in advection only in the -x direction. Therefore, both conduction and advection cause heat transfer in the x direction, whereas only conduction occurs in the y direction, and this difference in the heat transfer mechanism produces the asymmetric and symmetric temperature fields about the above-mentioned x and y lines, respectively.

The effect of speed is analyzed further in Fig. 12 to determine the dominant role of conduction or advection heat transfer mechanism in different ranges of the scanning speed, $V$. The maximum temperature in terms of $V$, $T_{max}(V) = T\left(\frac{L}{2}, D, H, \frac{L}{2V}\right)$, which occurs at the laser beam center, is plotted as a function of the scanning speed for different laser powers. $T_{max}(V)$ decreases as the scanning speed increases. Three ranges of the scanning speed are identified corresponding to three dominant modes of heat transfer mechanism, such as the conduction, advection and weakly heating regimes, using a temperature ratio to delineate these regimes. The temperature ratio is defined as $T_r(V) = \frac{T_{max}(V) - T_a}{T_{max}(V_{min}) - T_a}$, where $V_{min} = 0.1mm/s$ is the lowest velocity used in the experiments of this study. The dominant conduction, dominant advection and weakly heating regimes are classified by considering $T_r \geq 0.99$, $0.1 \leq T_r < 0.99$ and $T_r < 0.1$.

Optics EXPRESS

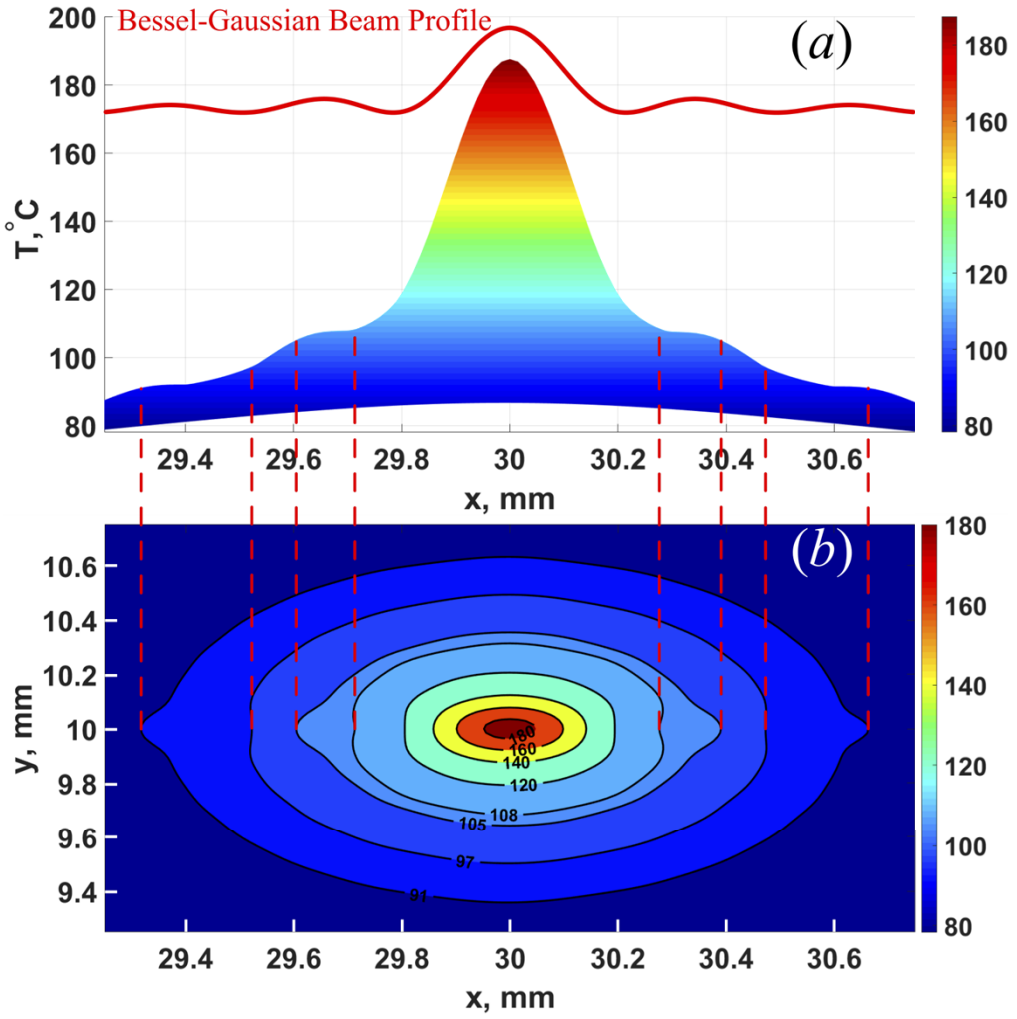


**Fig. 10.** Temperature distribution at the top surface of the substrate in the neighborhood of the laser beam center for a low scanning speed $V = 1$ mm/s: (a) Wavy temperature profile along the laser scanning line, and (b) Temperature contour with deformed leading and trailing edges. Process parameters for temperature calculation: $Q = 100$nL/min, ID = 51µm, $H_{ct} = 50\mu m$, $\theta_{in} = 40°$, P = 11.8W, $d_{ct} = 1.5mm$ and $D_L = 300\mu m$, D = 10mm (D* = 0.33) and t = 30s (t* = 0.5).

Optics EXPRESS

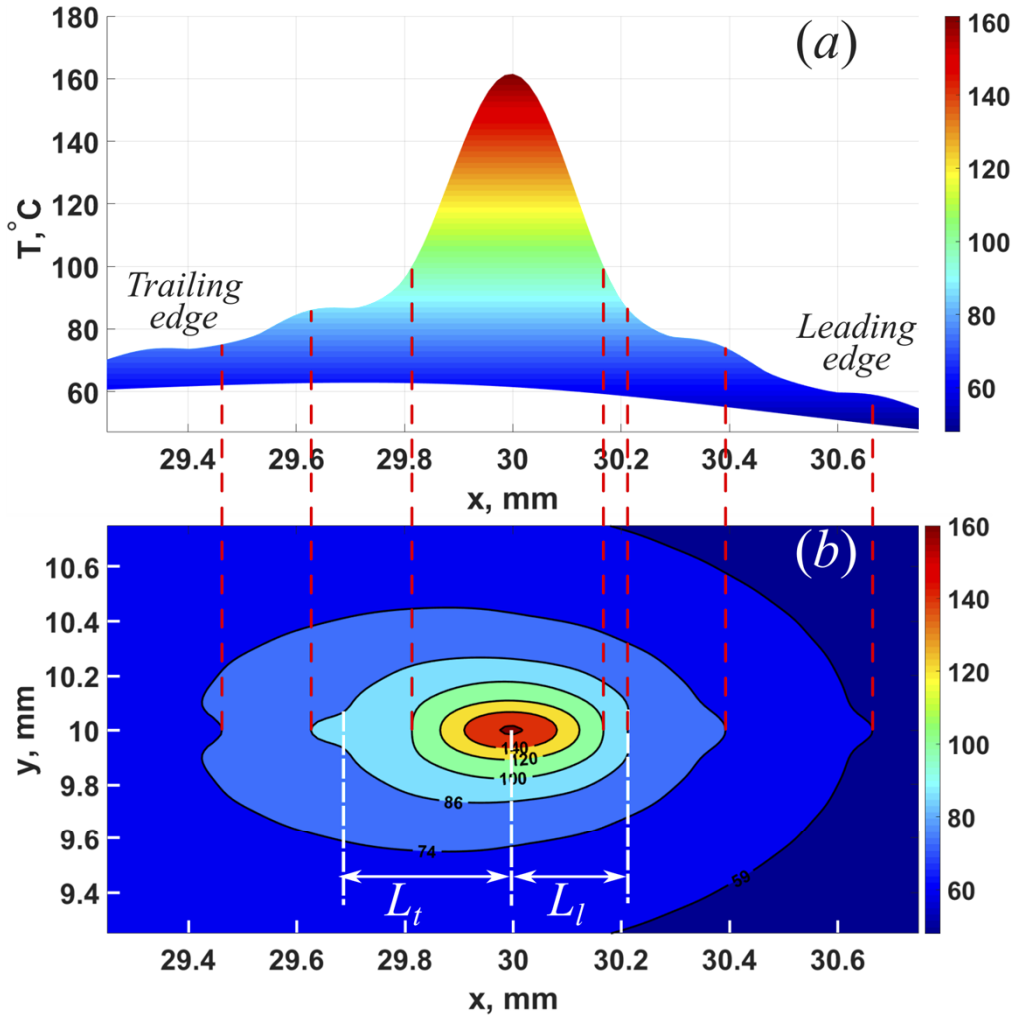


**Fig. 11.** Temperature distribution at the top surface of the substrate in the neighborhood of the laser beam center for a high scanning speed $V = 40$ mm/s: (a) Wavy temperature profile along the laser scanning line, and (b) Temperature contour with deformed leading and trailing edges. Process parameters for temperature calculation: $Q = 100$nL/min, ID = 51μm, $H_{ct} = 50\mu m$, $\theta_{in} = 40°$, P = 11.8W, $d_{ct} = 1.5mm$ and $D_L = 300\mu m$, D = 10mm (D* = 0.33) and t = 0.75s (t* = 0.5).

Optics EXPRESS

$T_{max}(V)$ is nearly constant with $T_r \geq 0.99$ for all powers and $0.1mm/s \leq V \leq 6mm/s$. This regime is characterized as the dominant conduction regime since the slow motion of the substrate allows sufficient time to reach a balance between the laser heating and the heat conduction. Thus a steady state is achieved, which also explains the reason for the maximum temperature to be nearly constant. $T_{max}(V)$, however, decreases significantly in the range $6mm/s < V \leq 50m/s$ . This regime is characterized as the dominant advection regime since the fast motion of the substrate decreases the laser heating time in the laser-irradiated region. Consequently, the spreading of heat by conduction is less than the heat carried away from the irradiated region by the moving substrate, and a steady state is reached in this case due to a balance between the laser heating and the heat advection. Finally, $T_{max}(V)$ tends to the room temperature asymptotically when $V > 50m/s$ since high scanning speeds decrease the laser-substrate interaction time and thus reduce the laser energy input to the substrate as the substrate passes through the laser-irradiated region. This high-speed scanning range is classified as the weakly heating regime. The substrate attains different temperatures in these three regimes of heating and the temperature, in turn, affects the sintering of the nanoparticles and the width of the deposited thin film.

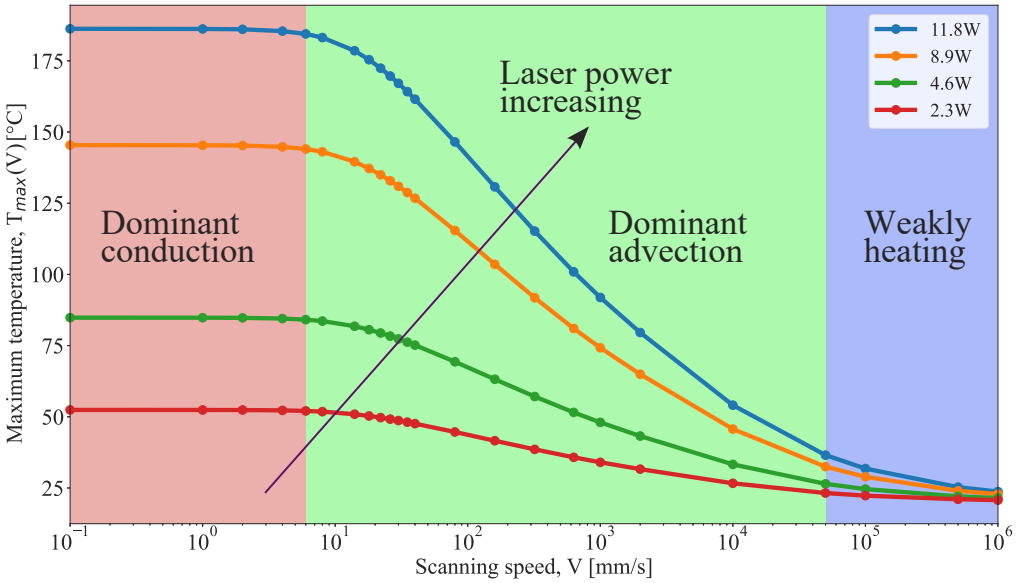


**Fig. 12.** Maximum temperature of the substrate in the dominant conduction, dominant advection and weakly heating regimes for different scanning speeds and laser powers. Process parameters for temperature calculation: $Q = 100$nL/min, ID = 51µm, $H_{ct} = 50\mu m$, $\theta_{in} = 40°$, $d_{ct} = 1.5mm$ and $D_L = 300\mu m$.

## 5. Conclusion

A Gaussian $CO_2$ laser is transformed to a Bessel-Gaussian beam using an axicon lens, a biconvex lens and a hollow parabolic mirror. A hollow collimated beam is incident on the mirror which reflects the beam as a hollow cone and the Bessel-Gaussian beam is formed at the focal plane of the mirror. The diffraction of light is analyzed using the Fresnel approximation to obtain an analytical expression for the irradiance distribution of the Bessel-Gaussian beam. This beam consists of a principal maximum irradiance at the laser beam center and subsidiary maxima that surround the principal maximum as rings. The irradiance distribution is applied as a heat flux boundary condition to a conduction model to analytically solve for the temperature distribution

Optics EXPRESS

in a moving silicon substrate on which Ag nanoparticles are sintered for depositing Ag lines. The temperature profile exhibits a wavy pattern like the wavy pattern of the irradiance distribution, resulting in noncongruent isotherms consisting of convex and concave tips. The Ag line width obtained from the thermal model is found to compare well with experimental data.

Symmetric and asymmetric isotherms are formed on the substrate surface depending on the distance of the laser beam from one of the edges of the substrate. The isotherms are perfectly symmetric when the laser scanning path coincides with the line of symmetry on the substrate surface, and asymmetric isotherms occur when the laser scanning path deviates from the line of symmetry. Another aspect of the thermal model is that the moving substrate introduces advection which influences the substrate temperature in addition to the conduction heat transfer mechanism. When the laser scanning speed relative to the substrate is low, the conduction effect is stronger than advection and the isotherms are symmetric in both the scanning (x) and transverse (y) directions running through the laser beam center. At higher scanning speeds, however, the advection effect is stronger than conduction and asymmetric and symmetric isotherms appear in the scanning (x) and transverse (y) directions, respectively. This direction-dependent characteristics appear out of the advection versus conduction effects. Since the substrate moves in the -x direction, the advection occurs only in this direction causing the asymmetric isotherms. Due to the absence of advection in the transverse direction, only conduction occurs in this direction resulting in the symmetric isotherms. When the scanning speed is increased further, the laser-matter interaction time decreases which lowers the energy input to the substrate and, consequently, the substrate temperature does not increase significantly. The heating regimes in these three ranges of the scanning speed can be classified as the dominant conduction, dominant advection, and weakly heating effects.

## Appendix A: derivation of $h_{Ag}$

In the heat transfer model, the thin Ag line is lumped as an additional heat transfer coefficient on top of the silicon substrate. Since the height of the Ag line in z direction, $H_{Ag}$ is about 1 μm which is much less than the dimensions in x and y directions, the governing equation of the Ag line can be simplified as a 1-D heat conduction problem:

$$\rho C_{p,\ Ag}\frac{\partial T}{\partial t} = k_{Ag}\frac{\partial^2 T}{\partial z^2} \tag{17}$$

Integration of Eq. (17) with respect to z yields

$$\rho C_{p,\ Ag}H_{Ag}\frac{\partial T}{\partial t} = I_h(x,y,H+H_{Ag}) - h_4(T(x,y,H+H_{Ag}) - T_a) - k(T)\frac{\partial T}{\partial z}|_{z=H} \tag{18}$$

The heat flux on the top surface of the substrate due to laser illumination with the effect of the Ag line can be expressed as:

$$k(T)\frac{\partial T}{\partial z} = I_h(x,y,H+H_{Ag}) - \rho C_{p,\ Ag}H_{Ag}\frac{\partial T}{\partial t} - h_4(T(x,y,H+H_{Ag}) - T_a) \tag{19}$$

Estimating $\frac{\partial T}{\partial t}$ as $\frac{T(x,y,H+H_{Ag})-T_a}{\delta t} = \frac{(T(x,y,H+H_{Ag})-T_a)V}{L}$, Eq. (19) can be rewritten as:

$$\begin{aligned} k(T)\frac{\partial T}{\partial z} &= I_h(x,y,H+H_{Ag}) - \left(\frac{\rho C_{p,\ Ag}H_{Ag}V}{L} + h_4\right)(T(x,y,H+H_{Ag}) - T_a) \\ &= I_h(x,y,H+H_{Ag}) - h_t(T(x,y,H+H_{Ag}) - T_a) \end{aligned} \tag{20}$$

where the effect of Ag line on the heat convection as a heat convection coefficient is lumped in $h_t$ as $h_t = h_{Ag} + h_4$ with $h_{Ag} = \frac{\rho C_{p,\ Ag}H_{Ag}V}{L}$.

Optics EXPRESS

## Appendix B: solution of the heat transfer equation

To solve the governing equation with the given boundary conditions and initial condition, Eqs. (14a-h) are nondimensionalized by assuming $x^* = x/L$, $y^* = y/W$, $z^* = z/H$, $t^* = tV/L$, $T^* = T/T_0$ and $k^* = k(T)/k(T_0)$, where $V$ is the scanning speed and $T_0$ is the approximated average temperature and will be used as the reference point for Taylor series expansion for linearizing the boundary conditions. Since $k(T)$ is a function of temperature, we further assume that $k(T) = p \cdot T^q$ to yield:

$$k^* = \frac{k(T)}{k(T_0)} = \left(\frac{T}{T_0}\right)^q = T^{*q} \tag{21}$$

To linearize the governing equation, define that $\frac{\partial T'^*}{\partial x_i^*} = k^* \frac{\partial T^*}{\partial x_i^*}$ and $T^{*q+1} = 1 + (q+1)T'^*$. Expand $T^{*q+1}$ at reference dimensionless temperature $T_r^*$:

$$T^* q + 1 = T_r^* q + 1 + (q+1)T_r^* q(T^* - T_r^*) = 1 + (q+1)T'^* \tag{22}$$

And yield that:

$$T^* = \frac{1}{(q+1)T_r^{*q}}[1 - T_r^{*q+1} + (q+1)T'^*] + T_r^* \tag{23}$$

where in our case, $T_r^*$ is defined to be 1. Since $T^* - T_a^*$ will be an important item in all boundary conditions, it is good to evaluate it first and express it in terms of $T'^*$

$$T^* - T_a^* = \frac{1}{(q+1)T_r^{*q}} - \frac{T_r^*}{q+1} + \frac{T'^*}{T_r^{*q}} + T_r^* - T_a^* = \frac{1}{T_r^{*q}}(T'^* + T_c^*) \tag{24}$$

with

$$T_c^* = T_r^* q\left(T_r^* - T_a^* + \frac{1 - T_r^* q + 1}{(q+1)T_r^* q}\right) \tag{25}$$

To linearize the convection boundary condition, we define

$$h_i(T - T_a) + \sigma\epsilon(T^4 - T_a^4) = [h_i + \sigma\epsilon(T^2 + T_a^2)(T + T_a)](T - T_a) = H_i(T - T_a) \tag{26}$$

where the subscript $i$ represent either the convection coefficient on the top surface or other surface. To further simplify the expression of $H_i$ ($i = 1,\ 2,\ 3,\ t$), $T$ is assumed to be the estimated average temperature $T_0$ to yield:

$$H_i = h_i + \sigma\epsilon(T_0^2 + T_a^2)(T_0 + T_a) \tag{27}$$

Defining $\Theta = T'^* + T_c^*$, the dimensionless governing equation, boundary conditions and initial condition can be expressed in terms of $\Theta$:

$$\frac{\partial^2\Theta}{\partial x^{*2}} + a^{*2}\frac{\partial^2\Theta}{\partial y^{*2}} + s^{*2}\frac{\partial^2\Theta}{\partial z^{*2}} = \frac{1}{Fo}\frac{\partial\Theta}{\partial t^*} \tag{28a}$$

$$\frac{\partial\Theta}{\partial x^*} = H_1^*\Theta \qquad at \qquad x^* = 0 \tag{28b}$$

$$\frac{\partial\Theta}{\partial x^*} = -H_1^*\Theta \qquad at \qquad x^* = 1 \tag{28c}$$

$$\frac{\partial\Theta}{\partial y^*} = H_2^*\Theta \qquad at \qquad y^* = 0 \tag{28d}$$

$$\frac{\partial\Theta}{\partial y^*} = -H_2^*\Theta \qquad at \qquad y^* = 1 \tag{28e}$$

Optics EXPRESS

$$\frac{\partial \Theta}{\partial z^*} = H_3^* \Theta \qquad at \qquad z^* = 0 \tag{28f}$$

$$\frac{\partial \Theta}{\partial z^*} = I^*(1 - Ref) - H_t^* \Theta \qquad at \qquad z^* = H \tag{28g}$$

$$\Theta(t^* = 0) = \frac{T_a^{*q+1} - 1}{q+1} + T_c^* \tag{28h}$$

where,

$$H_1^* = \frac{H_1 L}{k(T_0) T_r^{*q}} \tag{29a}$$

$$H_2^* = \frac{H_2 W}{k(T_0) T_r^{*q}} \tag{29b}$$

$$H_3^* = \frac{H_3 H}{k(T_0) T_r^{*q}} \tag{29c}$$

$$H_t^* = \frac{H_t H}{k(T_0) T_r^{*q}} \tag{29d}$$

$$I^* = \frac{I \cdot H}{k(T_0) T_r^{*q}} \tag{29e}$$

The dimensionless governing equation can be solved by integration transformation [35]. The integration kernels, $X$, $Y$, $Z$, the eigen values, $\lambda$ and the norms, $N$ in all directions can be determined from the homogeneous boundary conditions in $x$ and $y$ directions or the corresponding homogeneous boundary conditions in $z$ direction.

$$X(x^*) = H_1^* \sin(\lambda_{lx} x^*) + \lambda_{lx} \cos(\lambda_{lx} x^*) \tag{30a}$$

$$\tan \lambda_{lx} = \frac{2\lambda_{lx} H_1^*}{\lambda_{lx}^2 - H_1^{*2}} \tag{30b}$$

$$N_{lx} = \frac{1}{2}\left[H_1^* + (\lambda_{lx}^2 + H_1^{*2})\left(1 + \frac{H_1^*}{\lambda_{lx}^2 + H_1^{*2}}\right)\right] \tag{30c}$$

$$Y(y^*) = H_2^* \sin(\lambda_{my} y^*) + \lambda_{my} \cos(\lambda_{my} y^*) \tag{31a}$$

$$\tan \lambda_{my} = \frac{2\lambda_{my} H_2^*}{\lambda_{my}^2 - H_2^{*2}} \tag{31b}$$

$$N_{my} = \frac{1}{2}\left[H_2^* + (\lambda_{my}^2 + H_2^{*2})\left(1 + \frac{H_2^*}{\lambda_{my}^2 + H_2^{*2}}\right)\right] \tag{31c}$$

$$Z(z^*) = H_3^* \sin(\lambda_{nz} z^*) + \lambda_{nz} \cos(\lambda_{nz} z^*) \tag{32a}$$

$$\tan \lambda_{nz} = \frac{\lambda_{nz}(H_2^* + H_t^*)}{\lambda_{nz}^2 - H_2^* H_t^*} \tag{32b}$$

$$N_{nz} = \frac{1}{2}\left[H_3^* + (\lambda_{nz}^2 + H_3^{*2})\left(1 + \frac{H_t^*}{\lambda_{nz}^2 + H_t^{*2}}\right)\right] \tag{32c}$$

The transformation pairs are:

$$\begin{cases} \bar{\Theta}(\lambda_{lx}, \lambda_{my}, z^*, t^*) = \int_0^1 \int_0^1 \Theta(x^*, y^*, z^*, t^*) X(x^*) Y(y^*)\, dx^* dy^* \\ \Theta(x^*, y^*, z^*, t^*) = \sum_{l=0}^{\infty} \sum_{m=0}^{\infty} \bar{\Theta}(\lambda_{lx}, \lambda_{my}, z^*, t^*) \frac{X(x^*)}{N_{lx}} \frac{Y(y^*)}{N_{my}} \end{cases} \tag{33}$$

Optics EXPRESS

Take the integration in Eq. (33) and apply it to Eqs. (28a, f-h) to yield:

$$-(\lambda_{lx}^2 + a^{*2}\lambda_{my}^2)\bar{\Theta} + s^{*2}\frac{\partial^2\bar{\Theta}}{\partial z^{*2}} = \frac{1}{Fo}\frac{\partial\bar{\Theta}}{\partial t^*} \tag{34a}$$

$$\left.\frac{\partial\bar{\Theta}}{\partial z^*}\right|_{z^*=0} = H_3^*\bar{\Theta}(z^*=0) \tag{34b}$$

$$\left.\frac{\partial\bar{\Theta}}{\partial z^*}\right|_{z^*=1} = -H_t^*\bar{\Theta}(z^*=1) + f_{lm}(t^*) \tag{34c}$$

$$\bar{\Theta}(t^*=0) = \bar{\Theta}_i \tag{34d}$$

where,

$$\bar{\Theta}_i = \left(\frac{T_a^{*q+1}-1}{q+1} + T_c^*\right)\left[\sin\lambda_{lx} + \frac{H_1^*}{\lambda_{lx}}(1-\cos\lambda_{lx})\right]\left[\sin\lambda_{my} + \frac{H_2^*}{\lambda_{my}}(1-\cos\lambda_{my})\right] \tag{35}$$

$$f_{lm}(t^*) = (1-Ref)\int_0^1\int_0^1 I^*(x^*,y^*,t^*)X(x^*)Y(y^*)\,dx^*dy^* \tag{36}$$

Equation (34c) is the only nonhomogeneous boundary condition in $z$ direction, which can be homogenized by the following substitution:

$$\bar{\Theta}(\lambda_{lx},\lambda_{my},z^*,t^*) = \bar{\Theta}_1(\lambda_{lx},\lambda_{my},z^*,t^*) + \bar{\Theta}_2(\lambda_{lx},\lambda_{my},z^*,t^*) \tag{37}$$

where,

$$\bar{\Theta}_2(\lambda_{lx},\lambda_{my},z^*,t^*) = f_{lm}(t^*)\frac{H_3^*z^*+1}{H_3^*(1+H_t^*)+H_t^*} \tag{38}$$

Substitute Eq. (37) into Eqs. (34a-d) to yield:

$$-(\lambda_{lx}^2 + a^{*2}\lambda_{my}^2)(\bar{\Theta}_1+\bar{\Theta}_2) + s^{*2}\frac{\partial^2\bar{\Theta}_1}{\partial z^{*2}} = \frac{1}{Fo}\left(\frac{\partial\bar{\Theta}_1}{\partial t^*} + \frac{\partial\bar{\Theta}_2}{\partial t^*}\right) \tag{39a}$$

$$\left.\frac{\partial\bar{\Theta}_1}{\partial z^*}\right|_{z^*=0} = H_3^*\bar{\Theta}_1(z^*=0) \tag{39b}$$

$$\left.\frac{\partial\bar{\Theta}_1}{\partial z^*}\right|_{z^*=1} = -H_t^*\bar{\Theta}_1(z^*=1) \tag{39c}$$

$$\bar{\Theta}_1(t^*=0) = \bar{\Theta}_i - \bar{\Theta}_2(t^*=0) \tag{39d}$$

Since all the boundary conditions for $\bar{\Theta}_1$ are homogeneous boundary conditions. The integration transformation in $z$ direction is applied to $\bar{\Theta}_1$ using the following integral transformation pairs:

$$\begin{cases} \tilde{\Theta}_1(\lambda_{lx},\lambda_{my},\lambda_{nz},t^*) = \int_0^1 \bar{\Theta}_1(\lambda_{lx},\lambda_{my},z^*,t^*)Z(z^*)\,dz^* \\ \bar{\Theta}_1(\lambda_{lx},\lambda_{my},z^*,t^*) = \sum_{n=0}^{\infty}\tilde{\Theta}_1(\lambda_{lx},\lambda_{my},\lambda_{nz},t^*)\frac{Z(z^*)}{N_{nz}} \end{cases} \tag{40}$$

The governing equation and the initial condition can then be expressed as:

$$\lambda_{lmn}^2\tilde{\Theta} + \frac{d\tilde{\Theta}}{dt^*} = Fo\cdot s^{*2}\cdot\tilde{\Theta}_2 \tag{41a}$$

$$\tilde{\Theta}(t^*=0) = \tilde{\Theta}_i \tag{41b}$$

Optics EXPRESS

where,

$$\begin{aligned}\tilde{\Theta}_2 &= \int_0^1 \bar{\Theta}_2 Z(z^*)\, dz^* \\ &= \frac{f_{lm}(t^*)}{H_3^*(1+H_t^*)+H_t^*}\left[\frac{H_3^*}{\lambda_{nz}}(1-\cos\lambda_{nz})+\sin\lambda_{nz}\right] \\ &+ \frac{H_3^* f_{lm}(t^*)}{H_3^*(1+H_t^*)+H_t^*}\left[H_3^*\left(\frac{\sin\lambda_{nz}}{\lambda_{nz}^2}-\frac{\cos\lambda_{nz}}{\lambda_{nz}}\right)+\lambda_{nz}\left(\frac{\cos\lambda_{nz}-1}{\lambda_{nz}^2}+\frac{\sin\lambda_{nz}}{\lambda_{nz}}\right)\right]\end{aligned} \tag{42a}$$

$$\tilde{\Theta}_i = \int_0^1 \bar{\Theta}_i Z(z^*)\, dz^* = \bar{\Theta}_i\left[\sin\lambda_{nz}+\frac{H_3^*(1-\cos\lambda_{nz})}{\lambda_{nz}}\right] \tag{42b}$$

$$\tilde{\Theta} = \tilde{\Theta}_1 + \tilde{\Theta}_2 \tag{42c}$$

The ODE Eq. (41a) can be solve with Eq. (41b) to yield:

$$\tilde{\Theta}(t^*) = \tilde{\Theta}_i e^{-\lambda_{lmn}^2 t^*} + e^{-\lambda_{lmn}^2 t^*}\int_0^{t^*} Fo\cdot s^{*2}\cdot\lambda_{nz}^2\tilde{\Theta}_2(\tau)e^{\lambda_{lmn}^2\tau}\, d\tau \tag{43}$$

Thus, by applying Eq. (40) and Eq. (33) to $\tilde{\Theta}_1 = \tilde{\Theta} - \tilde{\Theta}_2$, $T'^*$ can be solved as:

$$\begin{aligned}T'^* = -T_c^* &+ \sum_{l=0}^{\infty}\frac{X(x^*)}{N_{lx}}\sum_{m=0}^{\infty}\frac{Y(y^*)}{N_{my}}\times \\ &\left[\bar{\Theta}_2+\sum_{n=0}^{\infty}\frac{Z(z^*)}{N_{nz}}\left(\tilde{\Theta}_i e^{-\lambda_{lmn}^2 t^*}-\tilde{\Theta}_2+e^{-\lambda_{lmn}^2 t^*}\int_0^{t^*} Fo\cdot\lambda_{nz}^2\cdot s^{*2}\tilde{\Theta}_2(\tau)e^{\lambda_{lmn}^2\tau}\, d\tau\right)\right]\end{aligned} \tag{44}$$

And the dimensionless temperature $T^*$ can then be solved from $T^{*q+1} = 1+(q+1)T'^*$ as:

$$T^* = [1+(q+1)T'^*]^{-(q+1)} \tag{45}$$

Finally, the dimensional temperature in the silicon substrate is

$$T = T_0\cdot[1+(q+1)T'^*]^{-(q+1)} \tag{46}$$

## Appendix C: evaluation of the integrations

In Eq. (36), $f_{lm}(t^*)$ integrate the dimensionless laser intensity multiplied by the eigen functions in $x$ and $y$ direction. Since the laser intensity is nonzero only within the laser spot, the integration can be evaluated by considering it within the laser spot and under a polar coordinate. The transformation between the Cartesian coordinate and the polar coordinate can be shown as:

$$\begin{cases} x = Vt + r_0 r^*\cos\theta \\ y = D + r_0 r^*\sin\theta \end{cases} \quad\rightarrow\quad \begin{cases} x^* = \frac{x}{L} = t^* + r^*\frac{r_0}{L}\cos\theta \\ y^* = \frac{y}{W} = D^* + r^*\frac{r_0}{W}\sin\theta \end{cases} \tag{47}$$

where $r_0$ represents the radius of the laser spot. $f_{lm}(t^*)$ can then be evaluated in terms of $r^*$ and $\theta$

$$\begin{aligned}f_{lm}(t^*) &= (1-Ref)\int_0^{2\pi}\int_0^1 I^*(r^*,\theta,t^*)X(x^*)Y(y^*)\frac{r_0^2}{L\cdot W}r^*\, dr^* d\theta \\ &= \frac{I_0\cdot H\cdot(1-Ref)}{k(T_0)T_r^{*q}L\cdot W}\int_0^{2\pi}\int_0^1\frac{1}{r^{*2}}\left[R_{out}^2 J_1^2\left(\frac{kR_{out}r}{z}\right)+R_{in}^2 J_1^2\left(\frac{kR_{in}r}{z}\right)e^{-4}\right. \\ &\left.-2R_{in}R_{out}J_1\left(\frac{kR_{in}r}{z}\right)J_1\left(\frac{kR_{out}r}{z}\right)\cos\left(\frac{R_{out}^2-R_{in}^2}{2z}-\frac{R_0\cos\beta}{\sin\alpha}\right)e^{-2}\right]\times\end{aligned}$$

Optics EXPRESS

$$\left\{H_1^* \sin\left[\lambda_{lx}\left(t^* + \frac{r_0}{L}r^*\cos\theta\right)\right] + \lambda_{lx}\cos\left[\lambda_{lx}\left(t^* + \frac{r_0}{L}r^*\cos\theta\right)\right]\right\} \times$$
$$\left\{H_2^* \sin\left[\lambda_{my}\left(D^* + \frac{r_0}{W}r^*\sin\theta\right)\right] + \lambda_{my}\cos\left[\lambda_{my}\left(D^* + \frac{r_0}{W}r^*\sin\theta\right)\right]\right\}\ r^* dr^* d\theta$$
$$= \frac{I_0 \cdot H \cdot (1 - Ref)}{k(T_0)T_r^{*q} L \cdot W} \int_0^1 \frac{1}{r^*}\left[R_{out}^2\, J_1^2\left(\frac{kR_{out}r}{z}\right) + R_{in}^2\, J_1^2\left(\frac{kR_{in}r}{z}\right)e^{-4}\right.$$
$$\left. -2R_{in}R_{out}J_1\left(\frac{kR_{in}r}{z}\right)J_1\left(\frac{kR_{out}r}{z}\right)\cos\left(\frac{R_{out}^2 - R_{in}^2}{2z} - \frac{R_0\cos\beta}{\sin\alpha}\right)e^{-2}\right] \times$$
$$\int_0^{2\pi}\left\{H_1^* \sin\left[\lambda_{lx}\left(t^* + \frac{r_0}{L}r^*\cos\theta\right)\right] + \lambda_{lx}\cos\left[\lambda_{lx}\left(t^* + \frac{r_0}{L}r^*\cos\theta\right)\right]\right\} \times$$
$$\left\{H_2^* \sin\left[\lambda_{my}\left(D^* + \frac{r_0}{W}r^*\sin\theta\right)\right] + \lambda_{my}\cos\left[\lambda_{my}\left(D^* + \frac{r_0}{W}r^*\sin\theta\right)\right]\right\}\ d\theta dr^* \tag{48}$$

Define

$$f_{lm}^{(1)}(r^*, t^*) = \int_0^{2\pi}\left\{H_1^* \sin\left[\lambda_{lx}\left(t^* + \frac{r_0}{L}r^*\cos\theta\right)\right] + \lambda_{lx}\cos\left[\lambda_{lx}\left(t^* + \frac{r_0}{L}r^*\cos\theta\right)\right]\right\} \times$$
$$\left\{H_2^* \sin\left[\lambda_{my}\left(D^* + \frac{r_0}{W}r^*\sin\theta\right)\right] + \lambda_{my}\cos\left[\lambda_{my}\left(D^* + \frac{r_0}{W}r^*\sin\theta\right)\right]\right\}\ d\theta$$
$$= \int_0^{2\pi}\sqrt{H_1^{*2} + \lambda_{lx}^2}\sin\left[\lambda_{lx}\left(t^* + \frac{r_0}{L}r^*\cos\theta\right) + \beta_1\right]$$
$$\times\sqrt{H_2^{*2} + \lambda_{my}^2}\sin\left[\lambda_{my}\left(D^* + \frac{r_0}{W}r^*\sin\theta\right) + \beta_2\right]\ d\theta \tag{49}$$

with

$$\tan\beta_1 = \frac{\lambda_{lx}}{H_1^*} \qquad and \qquad \tan\beta_2 = \frac{\lambda_{my}}{H_2^*} \tag{50}$$

Thus, $f_{lm}^{(1)}$ can be simplified as:

$$f_{lm}^{(1)}(r^*, t^*) = \frac{1}{2}\sqrt{H_1^{*2} + \lambda_{lx}^2}\sqrt{H_2^{*2} + \lambda_{my}^2}\int_0^{2\pi}\cos(A - B) - \cos(A + B)\ d\theta \tag{51}$$

where,

$$A = \lambda_{lx}\left(t^* + \frac{r_0 r^*}{L}\cos\theta\right) + \beta_1 \quad \text{and} \quad B = \lambda_{my}\left(D^* + \frac{r_0 r^*}{W}\sin\theta\right) + \beta_2 \tag{52}$$

Take $\int_0^{2\pi}\cos(A + B)d\theta$ as an example [36],

$$\int_0^{2\pi}\cos(A + B)d\theta = \int_0^{2\pi}\cos\left[(\lambda_{lx} + \lambda_{my})t^* + (\beta_1 + \beta_2) + \frac{\lambda_{lx}r_0 r^*}{L}\cos\theta + \frac{\lambda_{my}r_0 r^*}{W}\sin\theta\right]$$
$$= Re\left\{e^{i[(\lambda_{lx} + \lambda_{my})t^* + (\beta_1 + \beta_2)]}\int_0^{2\pi} e^{i\left(\frac{\lambda_{lx}r_0 r^*}{L}\cos\theta + \frac{\lambda_{my}r_0 r^*}{W}\sin\theta\right)}\ d\theta\right\}$$
$$= 2\pi J_0\left(\sqrt{\frac{\lambda_{lx}^2}{L^2} + \frac{\lambda_{my}^2}{W^2}}\ r_0 r^*\right)\cos[(\lambda_{lx} + \lambda_{my})t^* + (\beta_1 + \beta_2)] \tag{53}$$

With the same principle

$$\int_0^{2\pi}\cos(A - B)d\theta = 2\pi J_0\left(\sqrt{\frac{\lambda_{lx}^2}{L^2} + \frac{\lambda_{my}^2}{W^2}}\ r_0 r^*\right)\cos[(\lambda_{lx} - \lambda_{my})t^* + (\beta_1 - \beta_2)] \tag{54}$$

Optics EXPRESS

Thus,

$$f_{lm}^{(1)}(r^*,t^*) = \pi\sqrt{H_1^{*2}+\lambda_{lx}^2}\sqrt{H_2^{*2}+\lambda_{my}^2}\,J_0\left(\sqrt{\frac{\lambda_{lx}^2}{L^2}+\frac{\lambda_{my}^2}{W^2}}\,r_0 r^*\right)\times$$
$$\{\cos[(\lambda_{lx}-\lambda_{my})t^*+(\beta_1-\beta_2)]-\cos[(\lambda_{lx}+\lambda_{my})t^*+(\beta_1+\beta_2)]\} \quad (55)$$

$$f_{lm}(t^*) = \frac{I_0\cdot H\cdot(1-Ref)}{k(T_0)T_r^{*q}L\cdot W}\int_0^1\frac{1}{r^*}\left[R_{out}^2\,J_1^2\left(\frac{kR_{out}r}{z}\right)+R_{in}^2\,J_1^2\left(\frac{kR_{in}r}{z}\right)e^{-4}\right.$$
$$\left.-2R_{in}R_{out}J_1\left(\frac{kR_{in}r}{z}\right)J_1\left(\frac{kR_{out}r}{z}\right)\cos\left(\frac{R_{out}^2-R_{in}^2}{2z}-\frac{R_0\cos\beta}{\sin\alpha}\right)e^{-2}\right]\times f_{lm}^{(1)}(r^*,t^*)\,dr^* \quad (56)$$

Substitute Eq. (56) to Eq. (43) to yield:

$$\tilde{\Theta}(t^*) = \tilde{\Theta}_t e^{-\lambda_{lmn}^2 t^*} + Fo\cdot s^{*2}\lambda_{nz}^2\frac{(1-Ref)I_0H_3^*}{k(T_0)T_r^q}\frac{\pi}{L\cdot W}\sqrt{(H_1^{*2}+\lambda_{lx}^2)(H_2^{*2}+\lambda_{my}^2)}\cdot K_1\cdot K_2\cdot K_3 \quad (57)$$

where,

$$K_1 = \frac{H_3^*}{H_3^*(1+H_t^*)+H_t^*}\left[\frac{(1-\cos\lambda_{nz})}{\lambda_{nz}}+\frac{\sin\lambda_{nz}}{H_3^*}\right.$$
$$\left.+H_3^*\left(\frac{\sin\lambda_{nz}}{\lambda_{nz}^2}-\frac{\cos\lambda_{nz}}{\lambda_{nz}}\right)+\lambda_{nz}\left(\frac{\cos\lambda_{nz}-1}{\lambda_{nz}^2}+\frac{\sin\lambda_{nz}}{\lambda_{nz}}\right)\right] \quad (58)$$

$$K_2 = \int_0^1\frac{1}{r^*}\left[R_{out}^2\,J_1^2\left(\frac{kR_{out}r}{z}\right)+R_{in}^2\,J_1^2\left(\frac{kR_{in}r}{z}\right)e^{-4}-2R_{in}R_{out}J_1\left(\frac{kR_{in}r}{z}\right)\right.$$
$$\left.\times\,J_1\left(\frac{kR_{out}r}{z}\right)\cos\left(\frac{R_{out}^2-R_{in}^2}{2z}-\frac{R_0\cos\beta}{\sin\alpha}\right)e^{-2}\right]\times J_0\left(\sqrt{\frac{\lambda_{lx}^2}{L^2}+\frac{\lambda_{my}^2}{W^2}}\,r_0 r^*\right)dr^* \quad (59)$$

$$K_3 = e^{-\lambda_{lmn}^2 t^*}\int_0^{t^*}e^{\lambda_{lmn}^2\tau}\{\cos[(\lambda_{lx}-\lambda_{my})\tau+(\beta_1-\beta_2)]-\cos[(\lambda_{lx}+\lambda_{my})\tau+(\beta_1+\beta_2)]\}\,d\tau$$
$$= -e^{-\lambda_{lmn}^2 t^*}\frac{\lambda_{lmn}^2\cos(-\lambda_{my}D^*+\beta_1-\beta_2)+\lambda_{lx}\sin(-\lambda_{my}D^*+\beta_1-\beta_2)}{\lambda_{lmn}^4+\lambda_{lx}^2}$$
$$+\frac{\lambda_{lmn}^2\cos(\lambda_{lx}t^*-\lambda_{my}D^*+\beta_1-\beta_2)+\lambda_{lx}\sin(\lambda_{lx}t^*-\lambda_{my}D^*+\beta_1-\beta_2)}{\lambda_{lmn}^4+\lambda_{lx}^2}$$
$$+e^{-\lambda_{lmn}^2 t^*}\frac{\lambda_{lmn}^2\cos(\lambda_{lmn}^2 D^*+\beta_1+\beta_2)+\lambda_{lx}\sin(\lambda_{my}D^*+\beta_1+\beta_2)}{\lambda_{lmn}^4+\lambda_{lx}^2}$$
$$-\frac{\lambda_{lmn}^2\cos(\lambda_{lx}t^*+\lambda_{my}D^*+\beta_1+\beta_2)+\lambda_{lx}\sin(\lambda_{lx}t^*+\lambda_{my}D^*+\beta_1+\beta_2)}{\lambda_{lmn}^4+\lambda_{lx}^2} \quad (60)$$

**Funding.** U.S. Department of Energy (EE0008980).

**Acknowledgments.** This work was partially supported by the Office of Energy Efficiency and Renewable Energy (EERE), U.S. Department of Energy, under the Solar Energy Technologies Office Award Number DE-EE0008980. The authors thank J. F. Mousumi for the SEM images and EDX data in Fig. 6.

**Disclosures.** The authors declare no conflicts of interest.

**Data availability.** Data underlying the results presented in this paper are available in Ref. [28].

Optics EXPRESS

## References


1. T. Li, R. Kumar, and A. Kar, "Enhanced heating by microdroplet lens in nanoparticle electrospray laser deposition," J. Laser Appl. **33**(1), 012012 (2021).
2. J. Durnin, J. J. Miceli Jr, and J. H. Eberly, "Diffraction-Free Beams," Phys. Rev. Lett. **58**(15), 1499–1501 (1987).
3. J. Durnin, "Exact solutions for nondiffracting beams. I. The scalar theory," J. Opt. Soc. Am. A **4**(4), 651–654 (1987).
4. D. MCGloin and K. Dholakia, "Bessel beams: diffraction in a new light," Contemp. Phys. **46**(1), 15–28 (2005).
5. G. Indebetouw, "Nondiffracting optical fields: some remarks on their analysis and synthesis," J. Opt. Soc. Am. A **6**(1), 150–152 (1989).
6. V. Grillo, E. Karimi, G. C. Gazzadi, S. Frabboni, M. R. Dennis, and R. W. Boyd, "Generation of nondiffracting electron Bessel beams," Phys. Rev. X **4**(1), 011013 (2014).
7. G. Gbur and E. Wolf, "The Rayleigh range of Gaussian Schell-model beams," J. Mod. Opt. **48**(11), 1735–1741 (2001).
8. D. Zeng, W. P. Latham, and A. Kar, "Shaping of annular laser intensity profiles and their thermal effects for optical trepanning," Opt. Eng. **45**(1), 014301 (2006).
9. D. Zeng, W. P. Latham, and A. Kar, "Temperature distributions due to annular laser beam heating," J. Laser Appl. **17**(4), 256–262 (2005).
10. E. Castillo-Orozco, R. Kumar, and A. Kar, "Laser electrospray printing of nanoparticles on flexible and rigid substrates," J. Laser Appl. **31**(2), 022015 (2019).
11. E. A. Castillo, R. Kumar, and A. Kar, "Silver nanoparticle electrospray laser deposition for additive manufacturing of microlayers on rigid or flexible substrates," Proc. SPIE **10667**, 1066701 (2018).
12. P. Buffat and J. Borel, "Size effect on the melting temperature of gold particles," Phys. Rev. A **13**(6), 2287–2298 (1976).
13. T. Li, A. Kar, and R. Kumar, "Marangoni circulation by UV light modulation on sessile drop for particle agglomeration," J. Fluid Mech. **873**, 72–88 (2019).
14. T. H. Han, Y. Lee, M. R. Choi, S. H. Woo, S. H. Bae, B. H. Hong, J. H. Ahn, and T. W. Lee, "Extremely efficient flexible organic light-emitting diodes with modified graphene anode," Nat. Photonics **6**(2), 105–110 (2012).
15. M. Vomero, E. Castagnola, F. Ciarpella, E. Maggiolini, N. Goshi, E. Zucchini, S. Carli, L. Fadiga, S. Kassegne, and D. Ricci, "Highly stable glassy carbon interfaces for long-term neural stimulation and low-noise recording of brain activity," Sci. Rep. **7**(1), 40332 (2017).
16. B. D. Gates, "Flexible electronics," Science **323**(5921), 1566–1567 (2009).
17. P. Pathak, E. Castillo-Orozco, R. Kumar, A. Kar, and H. J. Cho, "Effect of laser power on conductivity and morphology of silver nanoparticle thin films prepared by a laser assisted electrospray deposition method," J. Laser Appl. **33**(1), 012034 (2021).
18. H. An, T. Habib, S. Shah, H. Gao, M. Radovic, M. J. Green, and J. L. Lutkenhaus, "Surface-agnostic highly stretchable and bendable conductive mxene multilayers," Sci. Adv. **4**(3), 118 (2018).
19. J. Thomas, P. Gangopadhyay, E. Araci, R. A. Norwood, and N. Peyghambarian, "Nanoimprinting by melt processing: an easy technique to fabricate versatile nanostructures," Adv. Mater. **23**(41), 4782–4787 (2011).
20. T. Y. Liu, H. C. Liao, C. C. Lin, S. H. Hu, and S. Y. Chen, "Biofunctional ZnO nanorod arrays grown on flexible substrates," Langmuir **22**(13), 5804–5809 (2006).
21. Y. M. Li, W. Kim, Y. G. Zhang, M. Rolandi, D. W. Wang, and H. J. Dai, "Growth of single-walled carbon nanotubes from discrete catalytic nanoparticles of various sizes," J. Phys. Chem. B **105**(46), 11424–11431 (2001).
22. M. S. Saleh, C. Hu, and R. Panat, "Three-dimensional microarchitected materials and devices using nanoparticle assembly by pointwise spatial printing," Sci. Adv. **3**(3), e1601986 (2017).
23. D. Shin, S. Yoo, H. Song, H. Tak, and D. Byun, "Electrostatic-force-assisted dispensing printing to construct high-aspect-ratio of 0.79 electrodes on a textured surface with improved adhesion and contact resistivity," Sci. Rep. **5**(1), 16704 (2015).
24. J. Qin, W. Zhang, S. Bai, and Z. Liu, "Study on the sintering and contact formation process of silver front side metallization pastes for crystalline silicon solar cells," Appl. Surf. Sci. **376**(15), 52–61 (2016).
25. J. Eymard, V. Barth, L. Sicot, B. Commault, A. Bettinelli, L. Basset, W. Favre, and A. Derrier, "CTMOD: A cell-to-module modelling tool applied to optimization of metallization and interconnection of high-efficiency bifacial silicon heterojunction solar module," In *AIP Conference Proceedings*, 2367(1), (AIP Publishing LLC, 2021), 020012.
26. A. J. Lopes, I. H. Lee, E. MacDonald, R. Quintana, and R. Wicker, "Laser curing of silver-based conductive inks for in situ 3D structural electronics fabrication in stereolithography," J. Mater. Process. Technol. **214**(9), 1935–1945 (2014).
27. K. S. Moon, H. Dong, R. Maric, S. Pothukuchi, A. Hunt, Y. Li, and C. P. Wong, "Thermal Behavior of Silver Nanoparticles for Low-Temperature Interconnect Applications," J. Elec. Mat. **34**(2), 168–175 (2005).
28. T. Li, "Laser-microdrop Interactions in Nanoparticle Deposition on Solid Substrates," University of Central Florida (2021), https://stars.library.ucf.edu/etd2020/724.
29. Y. Wang, S. Yan, A. T. Friberg, D. Kuebel, and T. D. Visser, "Electromagnetic diffraction theory of refractive axicon lenses," J. Opt. Soc. Am. A **34**(7), 1201–1211 (2017).
30. B. E. Saleh and M. C. Teich, *Fundamentals of photonics*, (John Wiley & Sons, 2019).
31. G. A. Slack, "Thermal conductivity of pure and impure silicon, silicon carbide, and diamond," J. Appl. Phys. **35**(12), 3460–3466 (1964).

Optics EXPRESS

32. T. Gao and B. P. Jelle, "Silver nanoparticles as low-emissivity coating materials," Transl. Mater. Res. **4**(1), 015001 (2017).
33. N. M. Ravindra, B. Sopori, O. H. Gokce, S. X. Cheng, A. Shenoy, L. Jin, S. Abedrabbo, W. Chen, and Y. Zhang, "Emissivity measurements and modeling of silicon-related materials: an overview," Int. J. Thermophys. **22**(5), 1593–1611 (2001).
34. T. L. Bergman, A. S. Lavine, F. P. Incropera, and D. P. DeWitt, *Introduction to heat transfer*, (John Wiley & Sons, 2011).
35. A. Kar and J. Mazumder, "Three-dimensional transient thermal analysis for laser chemical vapor deposition on uniformly moving finite slabs," J. Appl. Phys. **65**(8), 2923–2934 (1989).
36. I. S. Gradshteyn and I. M. Ryzhik, *Table of integrals, series, and products*, (Academic press, 2014).